View metadata, citation and similar papers at core.ac.uk
brought to you by CORE
provided by Sissa Digital Library

Scuola Internazionale Superiore di Studi Avanzati - Trieste
- ma per seguir virtute e conoscenza -

Rotational dynamics of molecular impurities solvated in ^{4}He clusters

a computational study based on reptation quantum Monte Carlo

Thesis submitted for the degree of
Philosophiæ Doctor

Candidate:
Stefano Paolini

Supervisors:
Prof. Stefano Baroni
and
Dr. Saverio Moroni

Contents

Introduction **1**

1 Doped Helium clusters and droplets **5**

1.1 Free rotor molecular spectra in ^{4}He nanodroplets 6

1.2 Spectroscopy of small ^{4}He clusters 9

1.2.1 Carbonyl sulfide 9

1.2.2 Carbon monoxide 10

1.2.3 Carbon dioxide and nitrous oxide 13

1.3 Previous theoretical studies 13

1.3.1 Hydrodynamic and two-fluid models 15

1.3.2 Rotational dynamics of small doped clusters: existing scenario 16

2 Reptation quantum Monte Carlo simulations **21**

2.1 Path Integral representation of the imaginary-time propagator . . . 22

2.2 Ground-state path integral Monte Carlo 24

2.2.1 Reptation quantum Monte Carlo 25

3 Technical details **29**

3.1 Doped cluster Hamiltonian 29

3.2 Sampling rotations 30

3.3 Trial functions 31

3.4 Extracting the absorption spectrum of doped He clusters 33

3.5 Projection-time and time-step biases 37

3.6 Computational costs and path sampling 38

3.7 Toward the nanodroplet regime 39

4 Understanding the relation between structure and dynamics: CO@He$_N$ 43
4.1 Ground state properties 43
4.2 Rotational spectrum 45
4.3 Structure and dynamics 48
4.4 Summary and discussion 52

5 Toward the nanodroplet regime 55
5.1 Molecule-atom interactions 55
5.2 Carbonyl sulfide 57
  5.2.1 Appraising the quality of intermolecular potentials 57
  5.2.2 Solvent density 58
  5.2.3 Effective rotational constants 59
5.3 Hydrogen cyanide 62
  5.3.1 Structural properties 63
  5.3.2 Rotational excitations 65
5.4 Fudged molecules 70
5.5 Summary and discussion 75

Conclusions and perspectives 77

A Pair density matrix approximation 79
A.1 Calculating the pair action for spherical potentials 80
A.2 Pair action approximation for anisotropic potentials 82

Bibliography 85

Acknowledgments 91

Introduction

Small molecules solvated in large ^{4}He clusters (nanodroplets) exhibit free-rotor-like spectra, though with a reduced rotational constant (hence with an increased molecular inertia) [1, 2]. This behavior has been interpreted as the vestiges of the superfluidity of the solvent in such extremely confined conditions [3]. The nearly-free rotation phenomenon raises the questions on how small a superfluid droplet could be, as well as on the causes of the renormalization of the molecular dynamics upon solvation and on the dependence of this effect on the cluster size [1]. Spectroscopic experiments have recently studied molecules in clusters with up to about twenty particles [4–7], showing that fingerprints of superfluidity can be found in these systems with just eight He atoms [4]. Available measurements, however, have not yet reached large enough sizes to show how the rotational dynamics of the solute in small clusters approaches that observed in nanodroplets. On the other hand, in the small-size regime non trivial effects of the solvent on the geometry of the system and on its dynamics may be found [5].

Spurred by experiments, considerable theoretical effort has been devoted at studying the rotational dynamics of ^{4}He solvated molecules. Several theoretical models have been proposed to explain the molecular inertia increase in nanodroplets [8–11]. Estimates of the latter can be obtained by using structural information derived from numerical simulations, yielding in various cases results in good agreement with observations [9–11]. Unfortunately, these models are suited, by construction, to the study of large clusters. For systems up to a few tens of He atoms, direct simulations of the rotational dynamics of embedded molecules exist, but the reliability of the results is not well established [11–14]. These calculations, in particular, contributed to originate the somewhat oversimplified view that the rotational dynamics of solvated heavy rotors would reach the nanodroplet regime well before the completion of the first solvation shell [2], whereas for light molecules the convergence would be much slower [14, 15]. This opinion, however, is partially contradicted by the latest experiments [6, 7, 16], thus demanding for further investigations.

Recent progresses in quantum many-body simulation techniques are now allowing for the determination of the low-lying excitations spectrum, as well as for the understanding of the relations between structure and dynamics in interacting bosons systems [17, 18]. For molecules solvated in He clusters, the scarcity of low-lying excited states makes it possible to extract information on the position and intensity of the spectral lines, from an analysis of the time series generated by quantum Monte Carlo (QMC) random walks [17–19]. Among the various QMC techniques, we have adopted reptation quantum Monte Carlo (RQMC) [17, 18], a path integral scheme which is particularly well suited to calculate ground state expectation values and imaginary-time correlation functions.

In this thesis, the rotational dynamics of several molecules solvated in He clusters has been simulated using RQMC. The small-size behavior of these systems has been studied in the case of clusters seeded with carbon monoxide ($CO@He_N$), for which the well known asymmetric top spectrum of the He-CO dimer [20] survives to relatively large sizes [5]. In our calculations, the features of the observed infrared spectra of $CO@He_N$ are accurately reproduced and interpreted in terms of the structural properties of the clusters.

Then, the problem of the convergence of the rotational dynamics of He solvated molecules to the nanodroplet regime is addressed. To this aim a heavy and a light molecule, in clusters with up to 50 He atoms, have been studied. We find that the approach to the asymptotic regime is slow in the former case, and fast in the latter. In contrast with common assumptions [2, 11], and in agreement with limited experimental evidence [6, 7, 16], our results demonstrate that interesting effects are present in the evolution of the rotational dynamics with the cluster size well beyond the completion of the first solvation shell. By useful computer experiments, we also show that the slow or fast approach to the asymptotic regime, as well as the increase of the molecular inertia upon solvation, are mainly determined by the strength and the anisotropy of the He-molecule interaction, more than by the molecular weight.

RQMC proved to be the most appropriate technique to study doped He clusters in the size range that we have explored. In order to study even larger systems we implemented the path sampling algorithm developed by Ceperley and Pollock for finite temperature simulations [21]. This method is expected to become more efficient than RQMC for large droplets [17] and we have studied the efficiency crossover with increasing the cluster size.

The thesis is organized as follows: in the first chapter we provide a short description of the scenario which frames our work. Some significant experiments are presented, together with the questions raised by them, the theoretical investigations they stimulated, and the open issues. The second chapter describes the reptation quantum Monte Carlo method and its theoretical foundations. Technical aspects (the choice of the trial functions, the procedure to calculate the cluster rotational energies) are discussed in third chapter. We also report some studies on the reptation algorithm. In the fourth chapter we apply RQMC for the interpretation of the infrared spectra of CO@He$_N$ [5]. The fifth chapter addresses the problem of the evolution of the rotational dinamics of He solvated rotors toward the nanodroplet regime; two paradigmatic cases, OCS@He$_N$ and HCN@He$_N$, are studied. Our conclusions are drawn in the last chapter.

Chapter 1

Doped Helium clusters and droplets

The great experimental interest in He droplets stems from their potential as spectroscopic matrices [1]. In spectroscopy, it is useful to cool the probed species in order to minimize the population of excited states, thus simplifying the spectra. In addition, the study of transient species, such as atoms, molecular radicals and ions, requires to prevent their uncontrolled aggregation [2]. Both these needs can be satisfied by trapping the species in low-temperature condensed media, the so-called matrices. Crystals of rare gases or hydrogen allow to reach the sub-Kelvin region ($T \leq 1$ K) [2]. The relatively strong interaction between the matrix and the solute species localizes and stabilizes the sample, but may result in considerable shifts or broadening of the spectral lines [1, 2].

The situation is quite different if one uses helium matrices, since helium does not solidify even down to absolute zero and has extremely weak interactions with foreign species. Moreover, thanks to its large quantum mechanical delocalization, liquid helium gently adapts itself to the solute [2]. However, because of the low molecular solubility in helium, molecular impurities quickly coagulate, thus preventing the use of liquid helium as a spectroscopic matrix in the bulk phase [1, 2]. The problem can be overcome by the cluster isolation technique [22], in which a beam of large He clusters (or *nanodroplets*), each containing $10^3 - 10^5$ atoms, passes through a chamber filled with the vapor of the foreign species and picks up in flight the impurity [1, 2, 22]. Isolation of dopant species inside or on the surface of the free droplets avoids their aggregation or precipitation. According to theoretical calculations, the rapid evaporation of atoms levels the temperature of ^{4}He droplets at $T \approx 0.4$ K, for times larger than about 10^{-4} sec [23]. In the case of ^{3}He droplets, the temperature is even lower ($T \approx 0.15$ K) [23]. Since the typical time of flight through the experimental apparatus is in the range of few milliseconds, the equilibrium temperature is reached before the pick-up process and it is maintained after the impact with the dopant, thanks to the evaporative cooling [1, 2]. In this ultra-cold and very gentle environment, the species are then probed downstream by laser spectroscopy [1, 2, 22]. The energy of the laser photon absorbed by the sample is relaxed in the droplet, leading to the evaporative loss of several hundreds of He atoms. The absorption is revealed by a mass spectrometer which monitors the droplets beam and detects the decrease in the droplet size [2].

Helium Nanodroplet Isolation (HENDI) spectroscopy is an extremely powerful technique, which provides highly resolved spectra, with small matrix shifts and broadenings (see below) [1, 2]. In addition, not only single molecules and unstable species, but also specifically tailored aggregates, assembled inside the droplets, can be studied [1, 2, 24].

1.1 Free rotor molecular spectra in ^{4}He nanodroplets

The first experimental evidence of the unique properties of ^{4}He droplets as spectroscopic matrix was reported in 1992 by Scoles *et al.* [25]. They observed infrared (IR) absorption lines of sulfur hexafluoride (SF_6) with a width much smaller than in other rare gas clusters. Later experiments by Toennies and collaborators [26] showed that the IR spectra of SF_6 presented a rotational fine structure. An analogue result was found later for carbonyl sulfide (OCS) [3], a linear molecule. For both SF_6 and OCS, the rotational peak spacing was significantly smaller than in gas-phase spectra.

In Fig. 1.1 [8] the absorption spectrum of OCS, measured in the gas phase at room temperature, is compared with that obtained in He droplets having mean size $\overline{N} \approx 3000$ atoms. Whereas the assignment of lines is not obvious at room temperature, the spectrum in ^{4}He droplets shows distinct free-rotor lines.

The rotational spectra of a linear molecule in the gas-phase are well described by the formula:

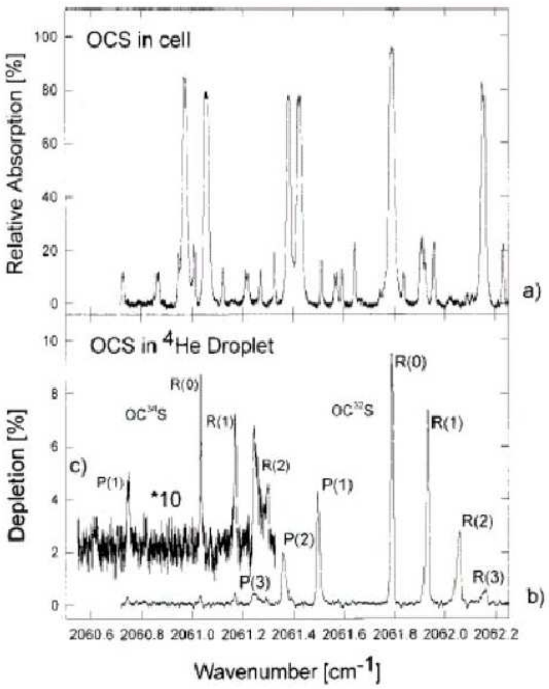

Figure 1.1: From Ref. [8]. Absorption spectrum of OCS molecule at $T = 300$ K (a) and in ^{4}He droplets (b). The mean droplet size is estimated to be $\overline{N} \approx 3000$. The factor 10 enlarged spectrum in the left hand corner (c) shows the results for the OC^{34}S isotope. The spectra are measured in the IR region of the C-O stretching vibration around 2062 cm^{-1}.

$$E_J = B_0 J(J+1) - D_0 J^2 (J+1)^2 \tag{1.1}$$

where J is the angular momentum, $B_0 = \hbar^2/2I_0$ is the rotational constant, I_0 is the moment of inertia, and D_0 is the centrifugal distortion constant, which accounts for the non rigidity of the molecule. When the molecule is solvated in ^{4}He droplets, the same relation holds, but the B values are smaller though of the same order as in the gas-phase. The centrifugal distortion constant, instead, is three or four orders of magnitude larger than in the gas-phase, thus indicating a significant floppiness of these systems [1]. For heavy molecules—with B_0 smaller than 1 cm^{-1}— B decreases by a factor $3-4$ upon solvation, while for light ones the reduction is much smaller [1]. From the line intensities, assuming a Boltzmann distribution, the droplet temperature can be determined. The resulting estimates

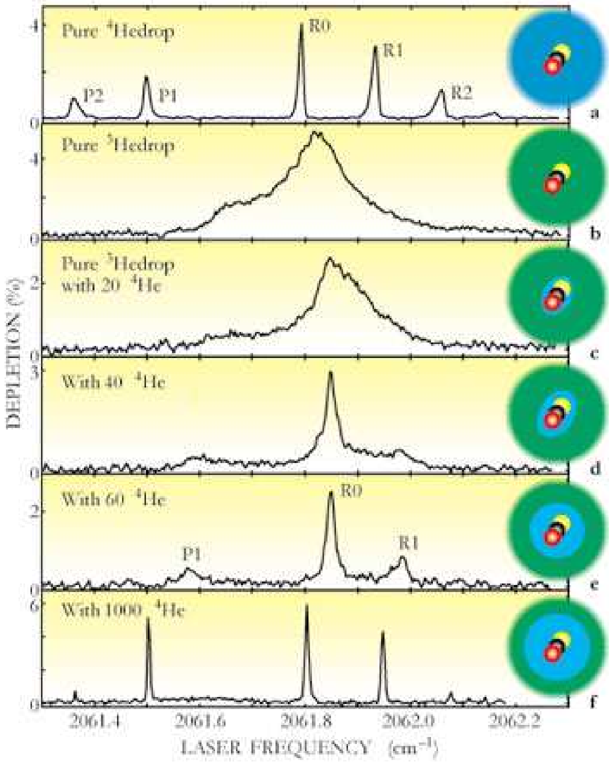

Figure 1.2: From Ref [27]. Infrared spectra of an OCS molecule in ^{4}He (panel a) and ^{3}He (panel b) clusters. Panels c-f: evolution of the spectra in ^{3}He, when an increasing number of ^{4}He atoms is added. Pictures on the right represent the OCS molecule in the clusters. ^{3}He and ^{4}He densities are indicated in green and blue, respectively.

give $T = 0.38$ K for ^{4}He droplets and $T = 0.15$ K for mixed ^{4}He/^{3}He ones (see below) [8], in agreement with theoretical predictions [23].

At the beginning, it was not clear whether the sharp rotational lines might simply be a consequence of the weak van der Waals He-molecule interactions, or they are related to the superfluidity of the environment. In 1998, Grebenev *et al.* [3] reported an experimental study of the spectra of OCS in both ^{4}He and ^{3}He droplets, demonstrating that the boson character of ^{4}He plays an essential role in the free rotation phenomenon. In Fig. 1.2 we report the spectra measured in Ref. [3]. In ^{4}He (Fig. 1.2 a) a well resolved rotational structure is observed. On the contrary, in ^{3}He (Fig. 1.2 b), only a broad band is found, just like in a classical liquid. The He-molecule interaction is the same for both isotopes. If the sharp rotational lines were a consequence of the weak van der Waals potential, then in ^{3}He, the lines should be even sharper because of the larger zero-point energy and lower temperature. The difference in the spectra, then, is a *microscopic* manifestation of superfluidity. According to theoretical calculations, in fact, at the temperature $T = 0.3 - 0.4$ K, pure and doped ^{4}He droplets are supposed to have a significant superfluid component, at least for $N \geq 40$ [28, 29]. On the contrary, the λ transition temperature is ~ 3 mK for ^{3}He, which is thus a normal fluid at the droplets temperature.

Ref. [3] provided also an indication on the minimum number of ^{4}He atoms needed to have a free rotation regime in nanodroplets. The authors found that ~ 60 He atoms around the OCS molecule (corresponding to about two solvation shells) are sufficient to provide resolved rotational spectra.

1.2 Spectroscopy of small ^{4}He clusters

The results of Grebenev *et al.* [3] pose the question on how small an ^{4}He cluster can be to show fingerprints of superfluidity. Recent refinements of experimental techniques allowed high-resolution spectroscopy on ^{4}He clusters with as few as $2 - 20$ atoms. In these experiments the sample is generated from a mixture of He atoms and gas-phase molecules [30], and the probed jet contains systems of different size. By tuning the pressure and the temperature in the production chamber, the relative abundance of a given complex is controlled, allowing for the assignment of individual lines to clusters with a well defined number of atoms [4, 5, 30]. The analysis of the lines intensities yields effective rotational temperature in the sub-Kelvin range [4, 5, 30].

1.2.1 Carbonyl sulfide

In 2003, Jäger and coworkers [4] studied OCS in small ^{4}He clusters (OCS@He$_N$), adding to the high resolution IR spectroscopy the direct observation of pure rotational transitions in the microwave (MW) region. The spectra of OCS@He$_N$ were measured up to about $N = 20$ and unambiguously assigned for $N = 2 - 8$ [4]. In this range, the combination of IR and MW data was used to derive the rotational constants B for the various sizes, N. In Fig. 1.3 we report the IR spectra observed

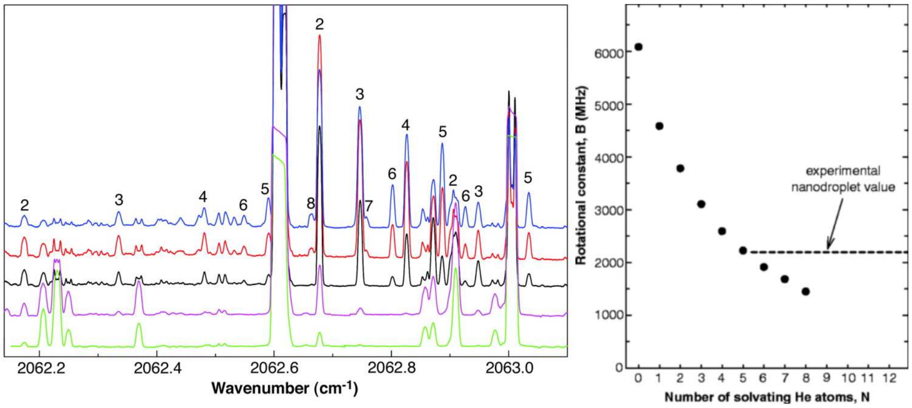

Figure 1.3: From Ref. [4]. Left panel: infrared spectra of OCS@He$_N$, observed in the region of the C-O stretching vibration of OCS ($\approx$ 2062 cm^{-1}). The spectra are stacked in order of increasing backing pressure [4]. Right panel: Rotational constant measured for $N = 1 - 8$. The dashed horizontal line refers to the B value observed in nanodroplets ($N \approx 10^4$). The circle at $N = 0$ is the gas-phase value $B_0 = 0.200$ cm^{-1}.

by Jäger *et al.* [4] and their results for $B(N)$.

By increasing the cluster size N, the rotational constant, B, decreases (indicating an increase in the effective moment of inertia) and, for $N = 6 - 8$, it undershoots the nanodroplet limit, $B_\infty = 0.073$ cm^{-1} (*i.e.* the value measured in large droplets [3]). According to the authors of Ref. [4], the turnaround of B to its asymptotic value (though not observed) has to be attributed to the partial decoupling of the first solvation shell He density from the molecular rotation. This hypothesis has been confirmed by quantum Monte Carlo calculations of the angular correlations between the molecular motion and the He-atom current [31]. The findings of Ref. [4] suggest that even He atoms in the first solvation shell may contribute to the superfluid fraction in the nanodroplets, thus providing the first experimental hint of the evolution of superfluidity at the atomic scale.

1.2.2 Carbon monoxide

Carbon monoxide (CO) is the second molecule which has been studied in ^{4}He matrices by N-resolved spectroscopy in the small size regime [5]. The infrared spectrum of CO@He$_N$ was measured in the region of the C-O stretching vibration (2145 cm^{-1}) [5]. Due to the low temperature ($T \sim 0.5$ K) [5] and to the large value of the rotational constant ($B_0 = 1.923$ cm^{-1}), only R(0) roto-vibrational transitions[1] were observed, thus preventing the disentanglement of the rotational and vibrational contributions.[2] However, the roto-vibrational patterns of CO@He$_N$ are less congested than in OCS@He$_N$ and lines have been reported up to $N = 21$, with clear assignments up to $N = 14$.

In Fig. 1.4 the infrared spectrum of CO@He$_N$ [5] is reported as a function of the cluster size N. The spectrum consists of two series of R(0) transitions. The lower energy one is indicated as a-type, the other as b-type. The series of b-type transitions starts off about seven times stronger for $N = 1$ and progressively looses intensity as N increases [5], until it disappears around $N = 7 - 8$. Around this size, just before it disappears, the b-type line seems to split in two. On the contrary, the a-type series gains strength from $N = 1$ to $N = 8$, and rapidly increases in energy for $7 \lesssim N \lesssim 12$, linking to the nearly free rotation observed at larger sizes. Analogously to the b-type series, around $N = 15$ the a-type line also seems to split. For $N \geq 15$ the line assignments become uncertain [5].

The spectrum of CO@He$_N$ can be better understood considering that the T-shaped He-CO complex has an asymmetric rotor spectrum [20], with two $R(0)$ lines, defined as a-type and b-type. The a-type line can be associated with the *end-over-end* rotation, *i.e.* the rotation of the vector from the CO center of mass to the He atom [20]. The b-type transition, instead, corresponds to the nearly-free rotation of the molecule in the complex. The two series in the spectrum of CO@He$_N$, smoothly correlate with the a-type and b-type $R(0)$ lines of the binary complex, and thus they have been indicated with the same notation.

The existence of two $R(0)$ lines in the spectra of CO@He$_N$, for clusters up to $N = 8$, was in a sense an unexpected result. For comparison, it has to be noticed that OCS@He$_N$, for $N = 1 - 2$, is an asymmetric rotor too, with more

---

[1] Transitions between vibrational levels $\nu = 0$ and $\nu = 1$ and between angular momentum states $J = 0$ and $J = 1$.

[2] The vibrational states of the solvated molecule are shifted by the presence of the matrix. Hence, the energy of the vibrational transition $\nu = 1 \leftarrow 0$ differs from that measured in the gas phase, and one observes a displacement of the center of the roto-vibrational band, ν_0, with respect to free molecule spectra. Such a displacement, which is generally small in He droplets, is called *vibrational shift*: $\Delta\nu_0 = \Delta E_{cluster} - \Delta E_{free}$, where $\Delta E_{cluster}$ and ΔE_{free} are the energies of the ν transition for a molecule in the cluster and in the gas phase, respectively [32].

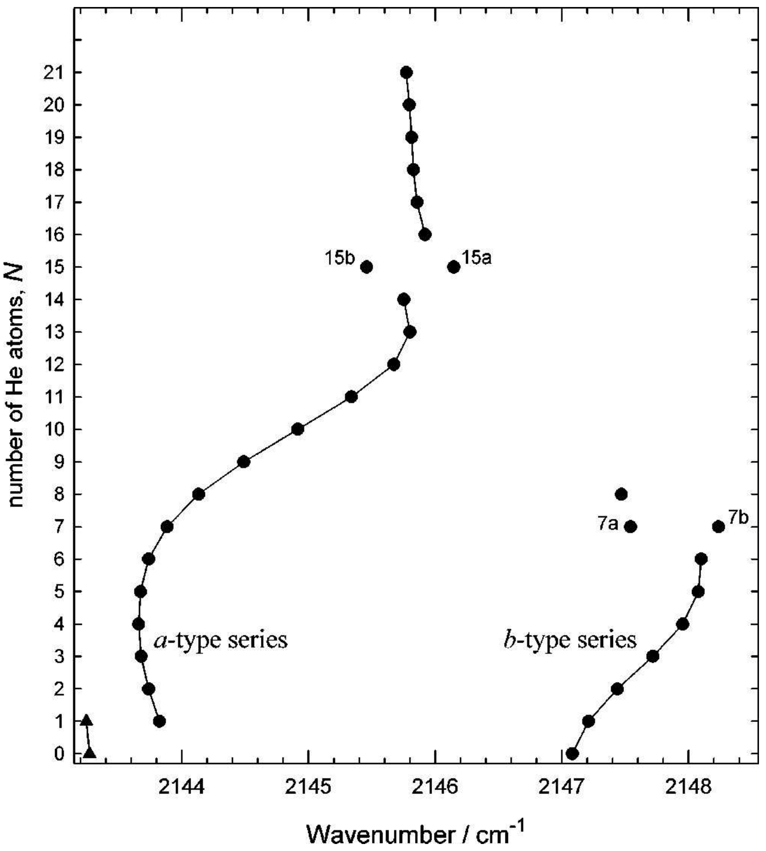

Figure 1.4: From Ref. [5]. Energies of the R(0) transitions of CO@He$_N$, as a function of the cluster size, N.

than one $R(0)$ transition in the spectra. The linear rotor behavior, however, is recovered almost immediately with increasing the cluster size [4]. On the contrary, for CO@He$_N$, J. Tang and A. R. W. McKellar [5] found that the asymmetric rotor spectra survived up to relatively large cluster sizes, thus indicating a non trivial role of the solvent in the system dynamics. Second, the a-type and b-type transitions derive continuously from the *end over end* rotation of the He-CO dimer and from the internal (free) rotation of CO in the complex, respectively. Since in large clusters the solvent should decouple from the molecule rotation, one would expect the b-type lines to grow in intensity and evolve into the free-rotor line of the nanodroplet limit. The fact that the opposite is observed was considered "puzzling" in Ref. [5]. Third, the authors speculate that the splitting at $N = 15$

could be caused by the crossing between the a-type series and a “dark states” one, due to other spectral excitations not revealed by the spectroscopic data [5]. In chapter 4 these problems will be discussed and rationalized in terms of the structure and the dynamics of the He matrix.

1.2.3 Carbon dioxide and nitrous oxide

Size-resolved molecular spectra in He clusters have been recently measured also for nitrous oxide ($N_2O@He_N$), both in the IR and MW regions, and for carbon dioxide ($CO_2@He_N$), only in the IR, for sizes up to $N = 12$ and $N = 17$, respectively [6, 7]. In Fig. 1.5 the rotational constant values for these two systems are compared with those of $OCS@He_N$. CO_2 and N_2O are, in several respects, analogous to OCS. Their rotational constants ($B_0 = 0.390$ cm^{-1} for CO_2 and $B_0 = 0.419$ cm^{-1} for N_2O) are close, even if larger, to that of OCS. These three molecules have also a similar interaction with the solvent, though with a greater strength in the case of N_2O (see Refs. [16, 33, 34] and references therein). However, B reduces differently in the three cases: $B_\infty/B_0 = 0.39$ for CO_2, $B_\infty/B_0 = 0.17$ for N_2O and $B_\infty/B_0 = 0.36$ for OCS [4, 6, 7]. A greater similitude, instead, is found in the small size behavior of the rotational constant, which shows an initial decrease in all the three cases. For CO_2 and N_2O, measurements arrive at sizes large enough to show a turnaround of B. The latter is interpreted in terms of transition from a van der Waals molecular complex to a full quantum solvation regime [7, 16]. It has also to be noticed that, at the largest explored size, the nanodroplet limit is not yet reached. Since $CO_2@He_N$ and $N_2O@He_N$ complete their first solvation shell around $N \sim 20$ [16, 34], the experiments suggest a nontrivial evolution of the rotational dynamics toward the asymptotic limit and also a non negligible role of the outer solvation shells in determining the convergence [6, 7].

1.3 Previous theoretical studies

Theoretical investigations on ^{4}He droplets have accompanied and, in several cases, preceded the experiments discussed so far. Using the liquid drop model, Stringari *et al.* [23] showed that at the low temperatures of the droplet, its internal regions

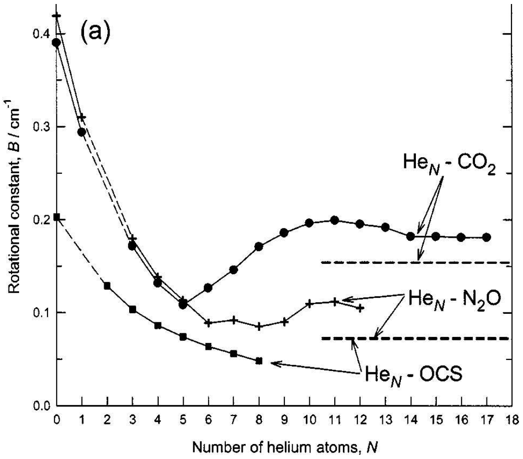

Figure 1.5: From Ref. [6]. Variation of the rotational constant B with the cluster size N, in the range $N = 0 - 17$. B values for CO$_2$@He$_N$, N$_2$O@He$_N$ and OCS@He$_N$ are obtained from Refs. [6], [7] and [4] respectively. The corresponding nanodroplets limit values are indicated by dashes lines.

are expected to be largely devoid of thermal excitations. In 1989, Sindzingre *et al.* [28] found a substantial superfluid fraction in pure ^{4}He droplets with 64 atoms, for temperatures below ~ 1.9 K. Studies based on the liquid drop model reported the appearance of the roton gap, typical of the bulk superfluid state, for ^{4}He clusters with about 70 atoms [35]. Density functional [36, 37] and quantum Monte Carlo calculations [38] predicted that atoms or molecules which interact strongly with helium, are located inside the droplets. As a result of the He-He and He-impurity interactions, modulations of the He density in a shell structure are found. On the contrary, ^{3}He [39] and alkali-metal atoms [40, 41] and their small clusters [42] are expected to reside on the droplet surface, producing a dimple on the latter [41, 42].

Further theoretical studies were spurred by the experimental results described in the previous section. Babichenko and Kagan [43] showed that the difference in the spectral line widths, found in ^{3}He and ^{4}He droplets, could be explained in terms of the different elementary excitations in the two quantum fluids, available to couple with the molecular rotation. After this work and prior to size-selective experiments, much effort has been devoted to the prediction of the B value in large droplets. In particular, two main models were proposed to explain the reduction of the rotational constant upon solvation: the *two-fluid model* [11], and the *hydrodynamical model* [9, 10]. The former is based on an early suggestion of Toennies *et al.* [3] that part of the He density follows the molecular rotation. The latter attributes a key role to the irrotational flow of the superfluid solvent around the rotating impurity. On the basis of given relations between structure and dynamics, the models can predict the nanodroplet B value starting from structural information. In this context, numerical simulations were mainly used to provide the structural input, but until 2003 few attempts have been done to simulate directly the cluster dynamics. In this section we give an account of the theoretical studies preceding our work.

1.3.1 Hydrodynamic and two-fluid models

The increase of the molecule inertia upon solvation was first explained by assuming that some of the solvent atoms would follow rigidly the molecule rotation [8, 26]. The model works for OCS and SF_6, but for light molecules the increase of the inertia is largely overestimated [1].

Grebenev *et al.* [3] introduced a more sophisticated two-fluid model, which follows the original Landau theory of superfluid ^{4}He [44, 45]. According to this model, the helium density would consist of *local* superfluid and normal components. Only the normal component, which is supposed to be large in the first solvation shell, would contribute to the molecular inertia [3]. Unfortunately, the authors do not provide any quantitative definition of this local normal fluid fraction. Kwon and Whaley [46], proposed to calculate the latter, following the scheme commonly adopted in path integral Monte Carlo (PIMC) simulations of ^{4}He systems [21, 28, 29, 47], where the Feynman's path integral expansion of the thermal density matrix is exploited to obtain the superfluid fraction [21]. In the approach of Kwon and Whaley [46], the *scalar* and *local* superfluid component, $\rho_s(\mathbf{r})$, is estimated from the imaginary-time exchange paths which are large relative to the system size [46].[3] The difference between the total He density and $\rho_s(\mathbf{r})$ provides the *non superfluid* density $\rho_{ns}(\mathbf{r})$ [46] (which is induced not only by thermal excitations, but also by the He-molecule interaction [11, 46]).

---

[3] Notice that the inertial response of helium to rotations is a second rank tensor. In 2003, Draeger and Ceperley defined a different local estimator for the superfluid density, which has the correct tensorial properties (see Ref. [47]). Following this approach, Kwon and Whaley have recently developed a tensorial local estimator, successfully tested on OCS (see Ref. [48]).

The increase in the molecular inertia is then calculated by integrating $\rho_{ns}(\mathbf{r})$ up to a cut off distance from the molecule, fixed at the end of the first solvation shell [11]. For heavy rotors (such as, e.g. SF_6 and OCS), this operation provides B estimates in good agreement with experimental values, but it is not viable in the case of light molecules [11]. This would be rationalized using the concept of *adiabatic following* [11]. Heavy molecules rotate slowly when excited and they usually have a stronger and more anisotropic interaction with the solvent. As a result of the combination of this two effects the non superfluid component would be dragged along by the molecular rotation. This effect would be greatly reduced in light rotors, both because they rotate faster and because their interaction with He atoms is usually more spherical [11, 49].

Callegari *et al.* [9, 10] have developed a hydrodynamical model, relying on two assumptions. The He density is supposed *(i)* to be fully superfluid, and *(ii)* to rearrange instantaneously around the rotating molecule by an irrotational flow. In other words, the density in the rotating frame of the molecule is constant and equal to that of the static case (the density profile is derived from Density Functional calculations) [9, 10]. The solvent rearrangement is defined as adiabatic following also in this context; notice that this expression has a different meaning with respect to the two-fluid model. The irrotational motion of the superfluid would generate a kinetic energy term proportional to the square of the angular velocity of the molecule, ω. The increase in the effective moment of inertia would then result from this hydrodynamical contribution to the total energy of the cluster as a function of ω. For light rotors, for which the hypothesis of adiabatic following does not hold [50], the model overestimates the inertia increase. For heavy rotors there is a good agreement with experimental values, and the discrepancies, which are at most by 30%, are ttributed to the uncertainties in the He solvation densities.

1.3.2 Rotational dynamics of small doped clusters: existing scenario

Recent progresses in Quantum Monte Carlo (QMC) methods are now allowing for a direct access to the dynamics of small molecules solvated in clusters with

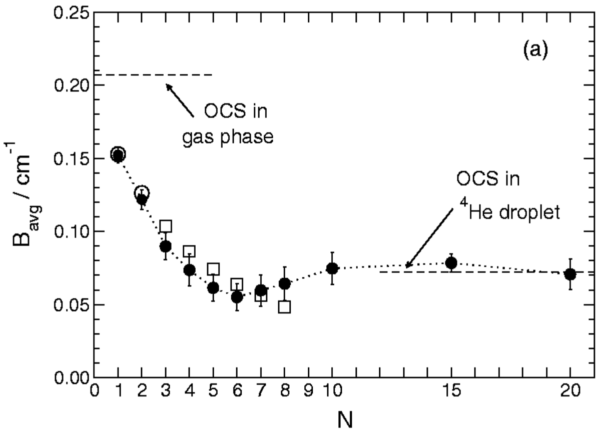

Figure 1.6: From Ref. [13]. Rotational constants B_{avg} for OCS@He$_N$ obtained from POITSE [19] (solid circles) and from experiments for $N = 1, 2$ [53, 54] (open circles) and $N = 3 - 8$ [4] (squares). The left dashed lines indicates the gas-phase value B_0; the right one corresponds to the large cluster limit, B_∞.

up to a few tens of He atoms [17, 19]. In particular it has now become possible to determine the spectrum of low-lying excitations of these systems [17, 19]. In this size range, still little explored experimentally, QMC simulations help to cover the gap between small clusters and nanodroplet regime [11, 13, 14]. Many investigations employed the *projector operator imaginary-time spectral evolution* (POITSE) technique [19], a development of diffusion Monte Carlo [51] (DMC), in which excited state energies are extracted from the inverse Laplace transform of the imaginary-time evolution of an initial state. To date, several molecules [11, 13, 14, 52], have been studied with POITSE simulations, even if some limitations of the method make the results not fully reliable.

Based on calculations for SF$_6$ [11] and, using POITSE, for OCS [13](see Fig. 1.6), Whaley and collaborators concluded that heavy rotors would approach the nanodroplet regime well before the completion of the first solvation shell [11, 13]. This fast convergence would be explained in terms of adiabatic following of the non superfluid density of the first solvation layer (see Sec. 1.3.1). The same argument would also account for the strong reduction of B observed in spectroscopic experiments [2, 11] ($B_\infty/B_0 = 0.36$ and 0.37 for OCS and SF$_6$, respectively).

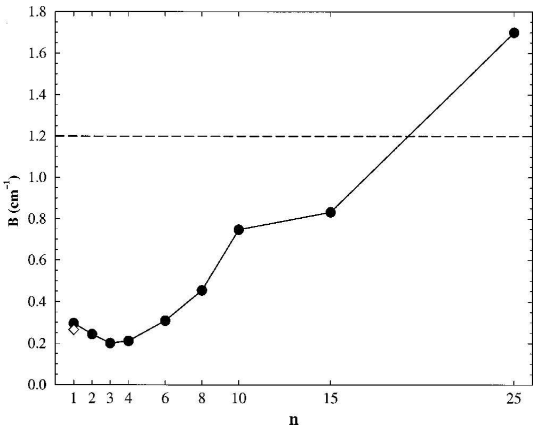

Figure 1.7: From Ref. [14]. Effective rotational constant B for HCN@He$_N$, as a function of the cluster size N. The B values are derived from POITSE calculations [14]. The rotational constant for $N = 1$ (diamond, Ref. [56]) and $N \approx 3000$ (dashed line, Ref. [50]) are also displayed.

Unfortunately, difficulties in the implementation of the POITSE method have required more than one study to improve the agreement of the calculations on OCS with available measurements [12, 13, 55]. Thus, it might not be worthless to carry out further investigations on the evolution of the OCS dynamics toward the asymptotic limit, and in fact, using a different computational approach, we found a significantly different behavior (see chapter 5). In addition, the cases of CO_2@He$_N$ and N_2O@He$_N$ contradict the proposed view (see Sec. 1.2.3). First of all, the rotational constant of these two heavy rotors show no signal of convergence to the asymptotic value within the completion of the first solvation shell. Second, given that for OCS there is *saturation* to almost full adiabatic following [49], this concept alone cannot explain the fact that N_2O undergoes a much stronger B reduction than the heavier OCS. These results suggest that solvent contributions to the dynamics of heavy rotors extend *beyond* the first solvation shell, and that the relation between molecular weight and effective inertia increase is less clear than expected.

Using POITSE, the rotational dynamics of He clusters seeded with hydrogen cyanide (HCN@He$_N$) was also studied [14], finding that at $N = 25$, beyond the completion of the first solvation shell ($N \approx 15$), B has not yet saturated to the nanodroplet limit ($B_\infty = 1.20$ cm^{-1}), and it stays significantly higher than the latter (see Fig 1.7). On the basis of these results and of a following study of HCN dynamics in the bulk limit [15], Zillich and Whaley proposed that the asymptotic B value for HCN derives primarily from coupling of the molecular rotation to the collective modes of the ^{4}He, and thus it is reached only for large enough clusters [15]. In this case, the much smaller B reduction experienced by light rotors with respect to heavy ones would result from the lack of adiabatic following. In Ref. [15], the rotational dynamics of light molecules solvated in He clusters is supposed to rely on a different physics with respect to that of heavy rotors. However, the hypothesis of the slow convergence to the asymptotic regime originates from the alleged large B value found for HCN@He$_{25}$ in Ref. [14], but this result clearly demands for further investigations. It has to be noticed, indeed, that for $N = 25$ the effective rotational constant is even larger than the gas-phase value ($B_0 = 1.47$ cm^{-1}). Because of the high isotropy of the He density profiles for these sizes [14], it seems difficult to explain such a result with an asymmetric reorganization of the solvent. Thus, such a large B value could be due to some inaccuracy in the calculations, as already supposed by the authors [14, 15]. In chapter 5, on the basis of our simulations, a completely different prediction will be presented.

Due to possible inaccuracies and to the mentioned discrepancies of the above results with available experiments [12–14, 52, 55], the view of a fast (slow) convergence for heavy (light) rotors seems somehow forced. As to the distinction between light and heavy molecules, it has also to be noticed that experimental evidence is not compatible with a simpler picture in which the lighter is the molecule, the smaller is the B reduction. There is not only the example of OCS and N_2O; also in the cases of CO, HCN and DCN, which have similar interactions with helium (even identical for the latter two molecules), a lighter mass corresponds to a stronger reduction upon solvation [50, 57]. These findings suggest that, maybe, something more (or something else) than the bare molecular inertia, plays a determinant role in the B reduction.

In the next chapter we will describe a more recent quantum Monte Carlo approach [17, 18], namely reptation quantum Monte Carlo (RQMC). For sizes up to several tens of He atoms, the method allows for an accurate description of clusters dynamics, and for a deeper understanding of its relation with the structure and, in some cases, the superfluidity of the system [31]. Using RQMC, several of the problems described here have been studied, obtaining interesting and, sometimes, unexpected results (see chapters 4 and 5).

Chapter 2

Reptation quantum Monte Carlo simulations

Let us consider a continuous quantum system described by the Hamiltonian $H = -\nabla^2 + V(\mathbf{R})$, where $\mathbf{R}$ is a D-dimensional vector denoting a configuration of the system and ∇ is the gradient with respect to $\mathbf{R}$. Let us indicate the ground state of H as Ψ_0. Static and dynamical properties of the system can be obtained by calculating, respectively, ground state expectation values

$$\langle \widehat{\mathcal{O}} \rangle = \frac{\langle \Psi_0 | \widehat{\mathcal{O}} | \Psi_0 \rangle}{\langle \Psi_0 | \Psi_0 \rangle}, \tag{2.1}$$

and time correlation functions

$$\mathcal{C}_{\widehat{\mathcal{O}}}(t) = \frac{\langle \Psi_0 | \widehat{\mathcal{O}}(t) \widehat{\mathcal{O}}(0) | \Psi_0 \rangle}{\langle \Psi_0 | \Psi_0 \rangle}. \tag{2.2}$$

of a suitably chosen quantum operator $\widehat{\mathcal{O}}$, where $\widehat{\mathcal{O}}(t) = e^{it\widehat{H}} \widehat{\mathcal{O}} e^{-it\widehat{H}}$.

In general, the evaluation of Eqs. 2.1 and 2.2 is not feasible for two reasons: *(i)* for interacting many-body systems, Ψ_0 is unknown; *(ii)* the time evolution of an operator in the Heisenberg representation, $\widehat{\mathcal{O}}(t)$, does not have a closed form. For static operators, (Eq. 2.1), the simplest solution to the first problem is to approximate Ψ_0 with an explicitly known trial wave function, Ψ_T, chosen as close as possible to the true ground state:

$$
\begin{aligned}
\langle\widehat{\mathcal{O}}\rangle &\approx \frac{\langle\Psi_T|\widehat{\mathcal{O}}|\Psi_T\rangle}{\langle\Psi_T|\Psi_T\rangle} \\
&= \frac{\int d\mathbf{R}|\Psi_T(\mathbf{R})|^2\mathcal{O}_T(\mathbf{R})}{\int d\mathbf{R}|\Psi_T(\mathbf{R})|^2} = \mathcal{O}_V,
\end{aligned} \tag{2.3}
$$

where $\mathcal{O}_T(\mathbf{R}) = \langle\mathbf{R}|\widehat{\mathcal{O}}|\Psi_T\rangle/\Psi_T(\mathbf{R})$. If $\widehat{\mathcal{O}}$ is local, $\langle\mathbf{R}|\widehat{\mathcal{O}}|\mathbf{R}'\rangle = \mathcal{O}(\mathbf{R})\delta(\mathbf{R}-\mathbf{R}')$, then $\mathcal{O}_T(\mathbf{R}) = \mathcal{O}(\mathbf{R})$, independent of Ψ_T. In the variational Monte Carlo method (VMC) [58], $\mathcal{O}_V$ is calculated by sampling configurations from the probability density $\pi(\mathbf{R}) = |\Psi_T(\mathbf{R})|^2/\int d\mathbf{R}'|\Psi_T(\mathbf{R}')|^2$, and then averaging $\mathcal{O}(\mathbf{R})$ over the sample. The sampling can be performed by a *generalized Metropolis algorithm* [58]. In particular, to explore the configuration space, one can generate a random walk according to the discretized Langevin equation [59]:

$$
\mathbf{R}_{k+1} = \mathbf{R}_k + \epsilon\mathbf{v}_D(\mathbf{R}_k) + \xi_k. \tag{2.4}
$$

where ϵ is the step of the time discretization, $\mathbf{v}_D = 2\nabla\left[\log\Psi_T(\mathbf{R})\right]$ is the drift velocity, and the ξ_k is a vector of Gaussian random numbers of zero mean value and variance 2ϵ.

VMC approach can be systematically improved by projecting out of Ψ_T its excited-state components by imaginary-time propagation: $|\Psi_0\rangle \propto \lim_{\beta\to\infty}|\Psi_\beta\rangle$, where $|\Psi_\beta\rangle = e^{-\beta\widehat{H}}|\Psi_T\rangle$. The ability to calculate $e^{-\beta\widehat{H}}$, would also solve the problem *(ii)*, provided one contents oneself of correlations in imaginary time, $\mathcal{C}_{\mathcal{O}}(\tau)$, where $\tau = -it$.

2.1 Path Integral representation of the imaginary-time propagator

In the coordinate representation, the expectation value of a local operator $\widehat{\mathcal{O}}$ on the state $|\Psi_\beta\rangle$ reads

$$
\langle\widehat{\mathcal{O}}\rangle_\beta = \frac{\langle\Psi_\beta|\widehat{\mathcal{O}}|\Psi_\beta\rangle}{\langle\Psi_\beta|\Psi_\beta\rangle}
$$

$$= \frac{\int d\mathbf{R}_1 d\mathbf{R}_2 d\mathbf{R}_3 \Psi_T(\mathbf{R}_1) G(\mathbf{R}_3, \mathbf{R}_1; \beta) G(\mathbf{R}_2, \mathbf{R}_3; \beta) \Psi_T(\mathbf{R}_2) \mathcal{O}(\mathbf{R}_1)}{\int d\mathbf{R}_1 d\mathbf{R}_2 \Psi_T(\mathbf{R}_1) G(\mathbf{R}_2, \mathbf{R}_1; 2\beta) \Psi_T(\mathbf{R}_2)}, \tag{2.5}$$

where

$$G(\mathbf{R}', \mathbf{R}; \beta) = \langle \mathbf{R}' | e^{-\beta \widehat{H}} | \mathbf{R} \rangle, \tag{2.6}$$

is the imaginary-time quantum propagator of the system.

Using the the identity $e^{-2\beta\widehat{H}} = (e^{-\epsilon\widehat{H}})^M$, with $\epsilon = 2\beta/M$, and a short time approximation, such as

$$\mathcal{G}(\mathbf{R}', \mathbf{R}; \epsilon) = (4\pi\epsilon)^{-D/2} e^{-\frac{(\mathbf{R}'-\mathbf{R})^2}{4\epsilon}} e^{-\frac{\epsilon}{2}[V(\mathbf{R}')+V(\mathbf{R})]} = G(\mathbf{R}', \mathbf{R}; \epsilon) + o(\epsilon^3) \tag{2.7}$$

for the quantum propagator, we arrive at a discretized *path integral* representation of ground state expectation values:

$$\langle \widehat{\mathcal{O}} \rangle_\beta \simeq \frac{\int d\mathbf{R}_0 \cdots d\mathbf{R}_M \Psi_T(\mathbf{R}_0) \prod_{i=0}^{M-1} \mathcal{G}(\mathbf{R}_{i+1}, \mathbf{R}_i; \epsilon) \Psi_T(\mathbf{R}_M) \mathcal{O}(\mathbf{R}_{\frac{M}{2}})}{\int d\mathbf{R}_0 \cdots d\mathbf{R}_M \Psi_T(\mathbf{R}_0) \prod_{i=0}^{M-1} \mathcal{G}(\mathbf{R}_{i+1}, \mathbf{R}_i; \epsilon) \Psi_T(\mathbf{R}_M)}, \tag{2.8}$$

where $\mathbf{R}_{\frac{M}{2}}$ is the mid configuration of the imaginary-time path $X = \{\mathbf{R}_0, \cdots, \mathbf{R}_M\}$. The same result holds for imaginary-time correlation functions, $\mathcal{C}_{\widehat{\mathcal{O}}}(\tau)$, with the difference that, in such a case, a single path entails a larger number of configurations, $M = (2\beta + \tau)/\epsilon$:

$$\mathcal{C}_{\widehat{\mathcal{O}};\beta}(\tau) \simeq \frac{\int d\mathbf{R}_0 \cdots d\mathbf{R}_M \Psi_T(\mathbf{R}_0) \Psi_T(\mathbf{R}_M) \prod_{i=0}^{M-1} \mathcal{G}(\mathbf{R}_{i+1}, \mathbf{R}_i; \epsilon) \mathcal{O}(\mathbf{R}_p) \mathcal{O}(\mathbf{R}_{p+l})}{\int d\mathbf{R}_0 \cdots d\mathbf{R}_M \Psi_T(\mathbf{R}_0) \Psi_T(\mathbf{R}_M) \prod_{i=0}^{M-1} \mathcal{G}(\mathbf{R}_{i+1}, \mathbf{R}_i; \epsilon)}, \tag{2.9}$$

where $p = \beta/\epsilon$ and $l = p + \tau/\epsilon$.

In the above expression, operator values are calculated at two points of the path separated by the imaginary-time interval τ. From now on the configurations $\mathbf{R}_0$, $\mathbf{R}_1$, $\cdots$, $\mathbf{R}_M$ will be also called *time slices* of the imaginary-time path X: the imaginary-time corresponding to the k-th time slice, $\mathbf{R}_k$, is $\tau_k = k \times \epsilon$.

The short time approximation of Eq. 2.7 is based on the Trotter decomposition [60] of the imaginary-time evolution operator, and it is known as the *primitive* *approximation* [21] (other and more accurate choices are possible, for instance, the *pair approximation* [21] (see next chapter). However, for the problems treated in this thesis the primitive approximation guarantees both accurate and efficient calculations). With this choice, the propagator is non-negative. Then, if the trial function is node-less, the expressions 2.8 and 2.9 for $\langle \widehat{\mathcal{O}} \rangle_\beta$ and $\mathcal{C}_{\widehat{\mathcal{O}};\beta}(\tau)$ have the form of statistical averages,

$$\langle F \rangle_\beta \simeq \frac{\int dX \pi[X] F[X]}{\int dX \pi[X]}, \tag{2.10}$$

of an appropriate estimator $F[X]$, over the probability density:

$$\pi[X] = \frac{\Psi_T(\mathbf{R}_0) \prod_{i=0}^{M-1} \mathcal{G}(\mathbf{R}_{i+1}, \mathbf{R}_i; \epsilon) \Psi_T(\mathbf{R}_M)}{\int d\mathbf{R}'_0 \cdots \mathbf{R}'_M \Psi_T(\mathbf{R}'_0) \prod_{i=0}^{M-1} \mathcal{G}(\mathbf{R}'_{i+1}, \mathbf{R}'_i; \epsilon) \Psi_T(\mathbf{R}'_M)} + o(\epsilon^2). \tag{2.11}$$

Eq. 2.10 is thus suitable for a Monte Carlo integration [58].

2.2 Ground-state path integral Monte Carlo

Ground-state path integral Monte Carlo methods [17, 21, 61] exploit precisely the discretized path integral representation of $e^{-\beta \widehat{H}} |\Psi_T\rangle$. The simulation amounts to generate a set of L paths $\{X_\alpha\}$, with $\alpha = 1, \cdots, L$, distributed according to $\pi[X]$. Estimates of ground state quantum expectation values are then obtained as averages over the paths. In the case of static operators, one simply accumulates the operator value in the central slice, $\mathbf{R}_{\frac{M}{2}}$, of the path. As to imaginary-time correlation functions, they can be evaluated in the central portion of the path, by accumulating the products of operator values in two time slices separated by $\tau = k\epsilon$: $\mathcal{C}_{\widehat{\mathcal{O}};\beta}(k\epsilon) = \langle \frac{1}{T/\epsilon-(k-1)} \sum_{i=0}^{T/\epsilon-k} \widehat{\mathcal{O}}(\beta+(i+k)\epsilon)\widehat{\mathcal{O}}(\beta+i\epsilon) \rangle$, where $\langle \cdots \rangle$ denotes an average over the sampled paths, T is the time length of their central portion (see Fig. 2.1), and $k = 0, \frac{T}{\epsilon}$.

The paths representative of $\pi[X]$ are sampled by using a generalized Metropolis algorithm [58], in which a move from X to Y is proposed according to a suitable *a priori* sampling distribution $W[Y, X]$ and then accepted with probability

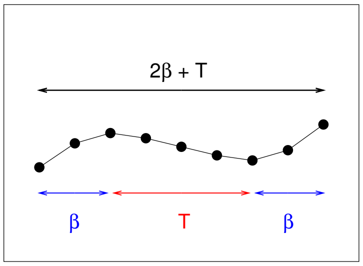

Figure 2.1: Graphical representation of an imaginary-time path. Filled circles correspond to the time slices of the reptile. The total imaginary-time associated with the path has length $2\beta + T$. β indicates the imaginary-time intervals which projects the trial function onto the ground state within the desired accuracy. T is the internal portion of the path, where the imaginary-time correlation functions are calculated. The path is discretized in time steps of length ϵ.

$$A[X,Y] = \min\left\{1, \frac{W[X,Y]\pi[Y]}{W[Y,X]\pi[X]}\right\}. \tag{2.12}$$

2.2.1 Reptation quantum Monte Carlo

In Eq. 2.12, if the sampling probability, $W[Y,X]$, satisfis the detailed balance condition, we could achieve acceptance 1. Hence, we search for a $W[Y,X]$ as close as possible to this condition. To this purpose, it proves useful to consider the importance-sampling Green's function [51] of the system

$$\tilde{G}(\mathbf{R}', \mathbf{R}; \epsilon) = \Psi_T(\mathbf{R}')G(\mathbf{R}', \mathbf{R}; \epsilon)\frac{1}{\Psi_T(\mathbf{R})}. \tag{2.13}$$

An explicit expression for $\tilde{G}$ is given by the approximation standardly used in diffusion Monte Carlo (DMC) [51]:

$$\tilde{G}(\mathbf{R}', \mathbf{R}; \epsilon) = G_d(\mathbf{R}', \mathbf{R}; \epsilon)e^{-\frac{\epsilon}{2}[\mathcal{E}_L(\mathbf{R}')+\mathcal{E}_L(\mathbf{R})]} + o(\epsilon^2), \tag{2.14}$$

where

$$G_d(\mathbf{R}', \mathbf{R}; \epsilon) = (4\pi\epsilon)^{-D/2}e^{-\frac{[\mathbf{R}'-\mathbf{R}-\epsilon\mathbf{v}_D(\mathbf{R})]^2}{4\epsilon}}, \tag{2.15}$$

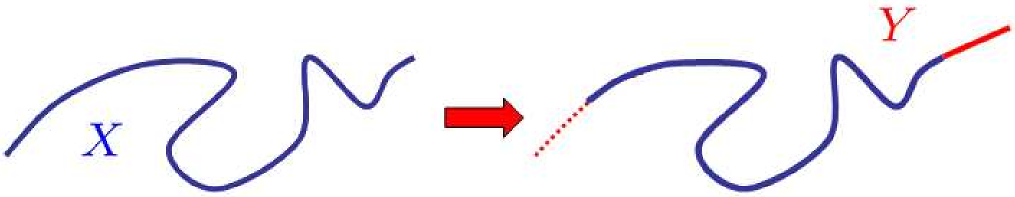

Figure 2.2: Graphical representation of the reptation algorithm. The old path, or snake, X is displayed in blue solid line. Red color is used for the new piece of the path. The dashed line indicates the portion of the old snake which is cut in the move.

and $\mathcal{E}_L(\mathbf{R}) = \frac{\hat{H}\Psi_T(\mathbf{R})}{\Psi_T(\mathbf{R})}$ is the so-called *local energy*. Using Eqs. 2.11, 2.13 and 2.14, the probability density of the paths can be written as

$$\begin{aligned}\pi[X] &= \frac{\Psi_T^2(\mathbf{R}_0)\prod_{i=0}^{M-1} G_d(\mathbf{R}_{i+1},\mathbf{R}_i;\epsilon)e^{-\frac{\epsilon}{2}[\mathcal{E}_L(\mathbf{R}_{i+1})+\mathcal{E}_L(\mathbf{R}_i)]}}{\int d\mathbf{R}'_0\cdots\mathbf{R}'_M\Psi_T^2(\mathbf{R}'_0)\prod_{i=0}^{M-1} G_d(\mathbf{R}'_{i+1},\mathbf{R}'_i;\epsilon)e^{-\frac{\epsilon}{2}[\mathcal{E}_L(\mathbf{R}'_{i+1})+\mathcal{E}_L(\mathbf{R}'_i)]}} + o(\epsilon) \\ &= \tilde{\pi}[X]e^{-\mathcal{S}[X]} + o(\epsilon), \qquad (2.16)\end{aligned}$$

where $\mathcal{S}[X] = \frac{\epsilon}{2}\sum_{i=0}^{M-1}[\mathcal{E}_L(\mathbf{R}_{i+1}) + \mathcal{E}_L(\mathbf{R}_i)]$. The factor $\tilde{\pi}[X]$ is the probability density of a variational path generated according to the the Langevin equation (Eq. 2.4), and thus it can be sampled directly by using the latter.

Given a quantum path, $X = \{\mathbf{R}_0, \cdots, \mathbf{R}_M\}$, the new path, Y, is conveniently proposed by adding one slice, generated through Eq. 2.4, at the head of the path, or *snake*, and cutting one slice from the tail: $Y = \{\mathbf{R}_1, \cdots, \mathbf{R}_{M+1}\}$ (the reverse move, in which a slice is added to tail and removed from the head with a change in the indexes, is also possible). Reptation quantum Monte Carlo method (RQMC) is named from this *reptation* or *slithering snake* algorithm [17] (see Fig 2.2). With such a choice $W[Y, X] = G_d(\mathbf{R}_{M+1}, \mathbf{R}_M; \epsilon)$, so that using the definition of $\pi[X]$ in Eq. 2.16, and the time-reversal properties of variational paths [17], the acceptance probability, Eq. 2.12, reduces to

$$A[X,Y] \cong \min\left\{1, \frac{e^{-\frac{\epsilon}{2}[\mathcal{E}(\mathbf{R}_{M+1})+\mathcal{E}(\mathbf{R}_M)]}}{e^{-\frac{\epsilon}{2}[\mathcal{E}(\mathbf{R}_1)+\mathcal{E}(\mathbf{R}_0)]}}\right\}. \qquad (2.17)$$

If the moves is accepted, the indexes of Y are relabeled from 0 to M (as for the choice of the slithering direction, see below).

Equation 2.17 shows both the strength and the weakness of the reptation algorithm: the acceptance probability depends only on the the local energy, apart from time discretization factors. In the ideal limit of $\Psi_T = \Psi_0$, $\mathcal{E}_L$ is a constant and each move is accepted with unit probability. In a more realistic case, when Ψ_T is not the exact ground state, the quality of the trial function can be improved by mean of optimization procedures. For a good trial function and systems not too large, as those studied in our work, local energy fluctuations are small, and RQMC is extremely efficient.[1]

Since RQMC displaces all the particles simultaneously at each step (*global moves*), in large systems, significant variations of $\mathcal{E}_L$, after a move, become more probable, causing a decrease in the acceptance rate. In this case algorithms based on one-particle moves, such as path integral ground state Monte Carlo (PIGS) [21, 61], guarantee a better scaling with the system size, since large local energy fluctuations are avoided (see next chapter).

The bounce algorithm

Our RQMC version uses the *bounce* algorithm [62], whereby if the moves is accepted, the next move is in the same direction, while, in case of rejection, the direction is reversed. Different solutions are possible. For instance, the slithering direction can be chosen randomly at each step. With this choice, it takes on average $\propto M^2$ steps (where M is the number time slices of the path) to refresh all the the slices [17]. The prefactor in this relation can be reduced by moving, at each MC step, a number of slices sampled with uniform deviate between 0 and a maximum value Δ, where Δ is chosen as to optimize the efficiency of the algorithm. Taking in to account the computational cost of such multiple moves, the net gain in CPU time is $\simeq \Delta$. The *bounce* procedure [62] avoids the search for the optimal Δ. More importantly this device allows one to save computational time, since expensive multiple moves are not rejected at the last step. In Ref. [62] it is demonstrated that the bounce algorithm samples the correct paths distribution, even though detailed balance is not satisfied.

---

[1] In our code, we do not use the propagator in the importance-sampling Green's function form (Eq. 2.14), but in the primitive approximation (Eq. 2.7). The two schemes, however, differ only for terms of the second order in ϵ. Thus the conclusions drawn in this paragraph remain valid.

Comparison with other methods

The use of the imaginary-time evolution operator is exploited in other ground state quantum Monte Carlo techniques. We first consider DMC, which is probably the most widely used approach for ground state simulations of continuous systems [51]. DMC is more efficient than RQMC for the calculation of the ground state energy, and, in the case of bosons, it provides an exact estimate of the latter. DMC, however, samples the mixed distribution $f = \Psi_T \Psi_0$, so that only mixed estimates are accessible for operators not commuting with the Hamiltonian [51]. Estimates are also biased by the *population control* associated with the branching scheme [51]. Finally, the dynamical variables of the random walk are single configurations and the imaginary-time "history" of the walker is not exploited to derive imaginary-time correlations. However, the latter, as well as biases-free estimates, can be obtained in any case, through the "forward walking" technique [63], but at the price of additional statistical fluctuations [17].

In comparison with DMC, RQMC samples imaginary-time paths and, thus, both ground state expectation values and imaginary-time correlation functions (Eqs.2.1 and 2.2) can be easily calculated without any systematic bias but those due to the finite projection time, β, and to the time step, ϵ [17, 18]. Sampling an explicitly known distribution, the discretized path integral expansion of $e^{-\beta \widehat{H}} \Psi_T$, allows one to employ a generalized Metropolis algorithm, avoiding branching [51], which may reduce the efficiency.

The imaginary-time path integral representation of quantum expectation values is also used in PIGS [21, 61]. For the systems we have studied, however, RQMC is more efficient, while PIGS becomes advisable to simulate larger clusters [28, 47]. In the next chapter, our implementation of PIGS algorithm will be shown and its performances will be compared to those of RQMC.

Chapter 3

Technical details

In this chapter several technicalities of our RQMC simulations are illustrated. First, we describe specific aspects related to the anisotropy of the He-molecule interaction, and, in particular, its effects on the quantum propagator, on the transition probability, and on the trial function. We also present the procedure to calculate the cluster rotational energies from imaginary-time correlation functions. In the last part, we dwell upon some general features of the RQMC algorithm (such as time-step and projection-time biases, computational time and efficiency scaling), as well as on some techniques which may be used to study very large systems.

3.1 Doped cluster Hamiltonian

Our clusters, which contain linear molecules such as CO, OCS, HCN, will be generically indicated as X@He$_N$, and they will be described through a realistic Hamiltonian, $\widehat{H}$, in which the N He atoms are treated as point particles and X as a rigid linear rotor:

$$\widehat{H} = -\frac{\hbar^2}{2M}\widehat{P}^2 - \frac{\hbar^2}{2m}\sum_{i=1}^{N}\widehat{p}_i^2 + \widehat{V}^{He-He} + \widehat{V}^{\Omega-He} + B_0\widehat{J}^2. \tag{3.1}$$

where m and $\widehat{p}_i$ are the mass and the linear momentum of He atoms, and M, B_0, $\widehat{P}$, $\widehat{J}$ are, respectively, the mass, the rotational constant, the linear and the angular momentum of the molecule. The He-He and the He-molecule potentials are assumed to be the sum of pair contributions: $\sum_{i<j}^{N} V^{He-He}(r_{ij})$ and

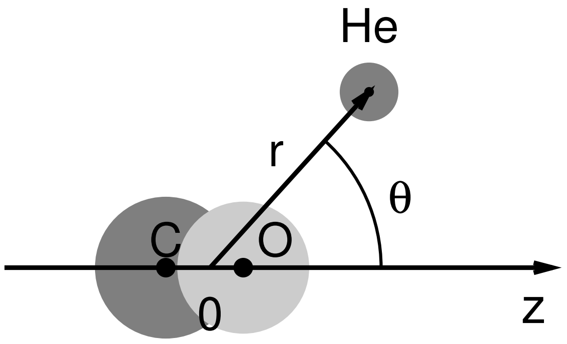

Figure 3.1: Graphical representation of the polar coordinates r and θ, used in the expression of the anisotropic He-molecule potential. As an example, the molecule was taken to be the carbon monoxide. C,O and He atoms are shown as filled circles. Here z coincides with the molecular symmetry axis.

$\sum_{i=1}^{N} V^{\mathrm{X}-He}(r_i, \theta_i)$ respectively, where $\mathbf{r}_i$ is the position of the i-th atom with respect to the center of mass of the molecule, $r_i = |\mathbf{r}_i|$, θ_i is the angle between $\mathbf{r}_i$ and the molecular axis, z (see Fig. 3.1), and r_{ij} is the distance between the i-th and the j-th He atoms. Our Hamiltonian does not depend on the rotor bond lengths, since we have assumed that inter and intra-molecular degrees of freedom are adiabatically decoupled. In fact, dopant vibrations and bound state energies of an He atom in the He-molecule potential well are of the order of some thousands and of a few tens of cm^{-1}, respectively. In our simulations, both the He-He and the He-molecule interactions are modeled by analytical expressions fitted to accurate *ab-initio* quantum-chemistry calculations. The potential energy surfaces (PES) that have been used for our systems are described in Refs. [20, 33, 64, 65].

3.2 Sampling rotations

For a system of N point particles plus a linear rotor, the quantum propagator contains a rotational term, whose exact expression is [66]:

$$G_{rot}(\hat{\mathbf{n}}, \hat{\mathbf{n}}'; \epsilon) = \langle \hat{\mathbf{n}} | e^{-\epsilon B_0 \hat{J}^2} | \hat{\mathbf{n}}' \rangle$$

$$= \sum_{J=0}^{\infty} \frac{2J+1}{4\pi} P_J(\hat{\mathbf{n}} \cdot \hat{\mathbf{n}}') e^{-\epsilon BJ(J+1)}, \tag{3.2}$$

where $\hat{\mathbf{n}}$ denotes the molecular axis versor. For small time steps, G_{rot} can be conveniently approximated by a Gaussian function of the angle α between $\hat{\mathbf{n}}$ and $\hat{\mathbf{n}}'$:

$$G_{rot}(\hat{\mathbf{n}}', \hat{\mathbf{n}}; \epsilon) \simeq \frac{1}{(4\pi B_0 \epsilon)^{1/2}} e^{-\frac{\alpha^2}{4\epsilon B_0}}. \tag{3.3}$$

This can be sampled directly by chosing randomly an axis orthogonal to $\hat{\mathbf{n}}$ and that rotating the latter around it, by an angle generated with probability $W_{rot} = G_{rot}$. Actually, the RQMC code that has been used is conceived for generic three-dimensional molecules and rotates them around their three principal axis of inertia. The orientation of the molecule is thus changed by successive rotations around the two principal axis orthogonal to $\hat{\mathbf{n}}$:

$$W_{rot}(\mathbf{n}', \mathbf{n}; \epsilon) \propto e^{-\frac{\varphi_1^2}{2\epsilon B_0}} \times e^{-\frac{\varphi_2^2}{4\epsilon B_0}} \times e^{-\frac{\varphi_1^2}{2\epsilon B_0}}, \tag{3.4}$$

where the different indexes of the rotation angles, φ_1 and φ_2, indicate rotations around different axis of inertia. The rotation φ_1 has been decomposed in two steps to reduce the effect of the non-commutativity of finite rotations around different axis.

3.3 Trial functions

For the trial wave function, Ψ_T, we use the standard Jastrow form [67]:

$$\Psi_T = \exp\left[-\sum_{i=1}^{N} \Phi_1(r_i, \theta_i) - \sum_{i<j}^{N} \Phi_2(r_{ij}) \right], \tag{3.5}$$

where Φ_1 and Φ_2 are known, respectively, as the He-molecule and the pair He-He pseudo-potentials. For Φ_2 we chose a functional form already used in accurate variational descriptions of bulk ^{4}He [68]:

$$\Phi_2(r) = \frac{p_1}{r^{p_2}} + p_3 e^{-p_4(r-p_5)^2}. \tag{3.6}$$

In the above and in the following formulas, the p_i's are parameters to be optimized (see below). Φ_1 is written as a sum of Legendre polynomials times radial functions:

$$\Phi_1(r, \theta) = \sum_l f_l(r) P_l(\cos\theta). \tag{3.7}$$

Retaining five or six terms in the sum is enough to represent even the most anisotropic situations treated in this work, namely, a ring of five He atoms tightly bound around the OCS molecular axis in correspondence with the principal minimum of the PES (see chapter 5). As for the radial function, $f_l(r)$, in the case of CO@He$_N$ and HCN@He$_N$, we have adopted the form [32]:

$$f_l(r) = \left[\log 2 \left(\frac{p_1}{r} \right)^5 p_2 r^{p_3} - p_4 \log r \right]. \tag{3.8}$$

The strongly anisotropic He-OCS interaction makes the radial density in OCS@He$_N$ clusters more structured than for CO and HCN. Hence, a more flexible expression for $f_l(r)$ has been used:

$$f_l(r) = \exp \left[\frac{p_1 + p_2 r^3 + p_3 r^5 + p_4 r^7}{r^5 + p_5 r^6} \right]. \tag{3.9}$$

Our trial function parameters, whose number is in the range of a few tens, have been optimized by standard minimization of the cluster variational energy, employing a correlated sampling scheme [58]. This approach has been preferred to the variance minimization [69] since, in our case, the latter might lead to trial functions ensuring a very small variance of the local energy, but poorly approximating the ground state (*e.g* a trial function representing a state in which all the He atoms are far away from each other and from the molecule). Even for the largest clusters, our optimization procedure requires only a small fraction of the total simulation time so that Ψ_T has been optimized independently for each size.

3.4 Extracting the absorption spectrum of doped He clusters

The absorption spectrum of a molecule solvated in a non polar environment is given by the Fourier transform of the autocorrelation function of its dipole, $\hat{\mathbf{d}}$:

$$\begin{aligned} I(\omega) &= \int_{-\infty}^{+\infty} \langle \Psi_0 | \hat{\mathbf{d}}(t) \cdot \hat{\mathbf{d}}(0) | \Psi_0 \rangle dt \\ &= 2\pi \sum_n |\langle \Psi_0 | \hat{\mathbf{d}} | \Psi_n \rangle|^2 \delta(E_n - E_0 - \omega), \end{aligned} \tag{3.10}$$

where Ψ_0 and Ψ_n are ground- and excited-state wave functions of the system and E_0 and E_n the corresponding energies. The real-time correlation function can be expressed as a sum of oscillating exponentials:

$$\langle \Psi_0 | \hat{\mathbf{d}}(t) \cdot \hat{\mathbf{d}}(0) | \Psi_0 \rangle = \sum_\omega I(\omega) e^{-i\omega t}. \tag{3.11}$$

Given that RQMC easily provides imaginary-time correlation functions as time correlation along the path, we analytically continue $\langle \Psi_0 | \hat{\mathbf{d}}(t) \cdot \hat{\mathbf{d}}(0) | \Psi_0 \rangle$ to imaginary time:

$$\langle \Psi_0 | \hat{\mathbf{d}}(-it) \cdot \hat{\mathbf{d}}(0) | \Psi_0 \rangle = \langle \hat{\mathbf{d}}(\tau) \cdot \hat{\mathbf{d}}(0) \rangle_{RW} \tag{3.12}$$

where the subscript RW underlines that the expectation value is obtained from the random walk sampling.

Continuation to imaginary-time transforms the oscillatory behavior of the real-time correlation function—which is responsible for the δ-like peaks in its Fourier transform—in a sum of decaying exponentials, whose decay constants are the excitation energies, and whose spectral weights are proportional to the absorption oscillator strengths, $|\langle \Psi_0 | \hat{\mathbf{d}} | \Psi_n \rangle|^2$:

$$\langle \hat{\mathbf{d}}(\tau) \cdot \hat{\mathbf{d}}(0) \rangle_{RW} = \sum_n |\langle \Psi_0 | \hat{\mathbf{d}} | \Psi_n \rangle|^2 e^{-\varepsilon_n \tau} \tag{3.13}$$

where $\varepsilon_n = E_n - E_0$. Dipole selection rules imply that only states with $J = 1$ can be optically excited from the ground state:

$$\langle J'M'|\hat{\mathbf{d}}|J=0\rangle = 0 \qquad \text{if} \qquad J' \neq 1. \tag{3.14}$$

The dipole of a linear molecule in a non polar environment, is oriented along its axis, so that the optical activity is essentially determined by the autocorrelation function of the molecular orientation versor, $\hat{\mathbf{n}}$.

The energies of the transitions to excited states with higher angular momenta J can be easily obtained from the multipole correlation function $c_J(\tau)$, defined as the imaginary-time correlations of the Legendre polynomials,

$$\begin{aligned} c_J(\tau) &= \Big\langle P_J(\hat{\mathbf{n}}(\tau)\cdot\hat{\mathbf{n}}(0)) \Big\rangle_{RW} \\ &= \left\langle \left[\frac{4\pi}{2J+1} \sum_{M=-J}^{M=J} Y^*_{JM}(\hat{\mathbf{n}}(\tau)) Y_{JM}(\hat{\mathbf{n}}(0)) \right] \right\rangle_{RW} , \end{aligned} \tag{3.15}$$

given that

$$\langle J'M'|Y_{LM}(\mathbf{d})|J=0\rangle = 0 \qquad \text{if} \qquad J' \neq L \qquad \text{or} \qquad M' \neq M. \tag{3.16}$$

The energies, ε^J_n, and the corresponding spectral weights, A^J_n, for rotational transitions from the ground state to states with angular momentum J can be derived from a fit of $c_J(\tau)$ to a sum of decaying exponentials:

$$c_J(\tau) \approx \sum_n A^J_n e^{-\varepsilon^J_n \tau}. \tag{3.17}$$

Generally speaking, the usefulness of this representation for obtaining the dynamical properties from quantum simulations is rather limited, because the calculation of the spectrum from imaginary-time correlation functions requires to carry out an inverse Laplace transform, a notoriously ill-conditioned problem [70]. In the case of doped He clusters, however, the situation is not so bad, because very few excited states contribute to $c_J(\tau)$. In fact, if the solvated molecule was isolated only one rotational state would contribute to $c_J(\tau)$ which would have therefore the form of a single exponential. Furthermore, the interaction between the solvent matrix and the solute molecule is rather weak, so that this single-exponential picture is only slightly perturbed. Last and most important, the bosonic nature of the quantum solvent determines a low density of low-lying excitations. As a consequence of the scarcity of low-lying excitations available to couple with the molecular rotation, the spectrum consists of very few peaks, well separated in energy, which nearly exhaust the entire spectral weight. The positions and the intensity of the spectral lines can then be reliably extracted by the multiexponential fit in Eq. 3.17.

The reliability of our fitting procedure is assessed by checking how our results depend on the number of exponentials, n, entering the fit. While a single exponential is not enough to fit the data, by increasing n one quickly reaches a situation of over-fitting, in which the data are equally well fitted by vastly different spectra. This is the manifestation of the mentioned fact that the inverse Laplace transform is an ill-conditioned problem.

In particular, we determine the excitation energies and the spectral weights when, adding a new exponential, three conditions are fulfilled: *(i)* the χ^2 is acceptable; *(ii)* energies and spectral weights remain stable; *(iii)* statistical errors are small enough. In Fig. 3.2 we report three paradigmatic situations, regarding the $c_{\hat{\mathbf{n}}}(\tau)$ correlation functions of HCN@He$_N$, for $N = 1, 10, 20$. For $N = 1$ the first requirement is satisfied starting from $n = 2$. With $n = 3$ and $n = 4$ *(ii)* and *(iii)* are also verified and, thus the multi-exponential fit provides reliable results. For $N = 10$, the condition *(ii)* is satisfied for $n = 3, 4$ within the statistical errors, but the latter are relatively large, particularly on the energies. Hence, the third condition is not fully verified, indicating that longer simulations are needed. The $N = 10$ cluster is thus a limiting case, where the information extracted from the multiexponential fit is not too robust. For $N = 20$, all the conditions are satisfied quite well for $n = 2$ and $n = 3$. The spectral function contains a single dominant exponential, while the others have small weights and very high energies.

The accuracy of the estimate of the rotational energies and of the corresponding spectral weights also depends on the length of the imaginary-time used to calculate the time correlations. The internal portion of the path, whose time length is T (see chapter 2), has to be long enough so that the multiexponential fit can clearly distinguish the lowest modes in the spectrum. Fig. 3.3 reports the two lowest rotational energies, ε_1 and ε_2, and the corresponding spectral weights as extracted from the correlation function $c_{\hat{\mathbf{n}}}(\tau)$ of CO@He$_1$, for different values of

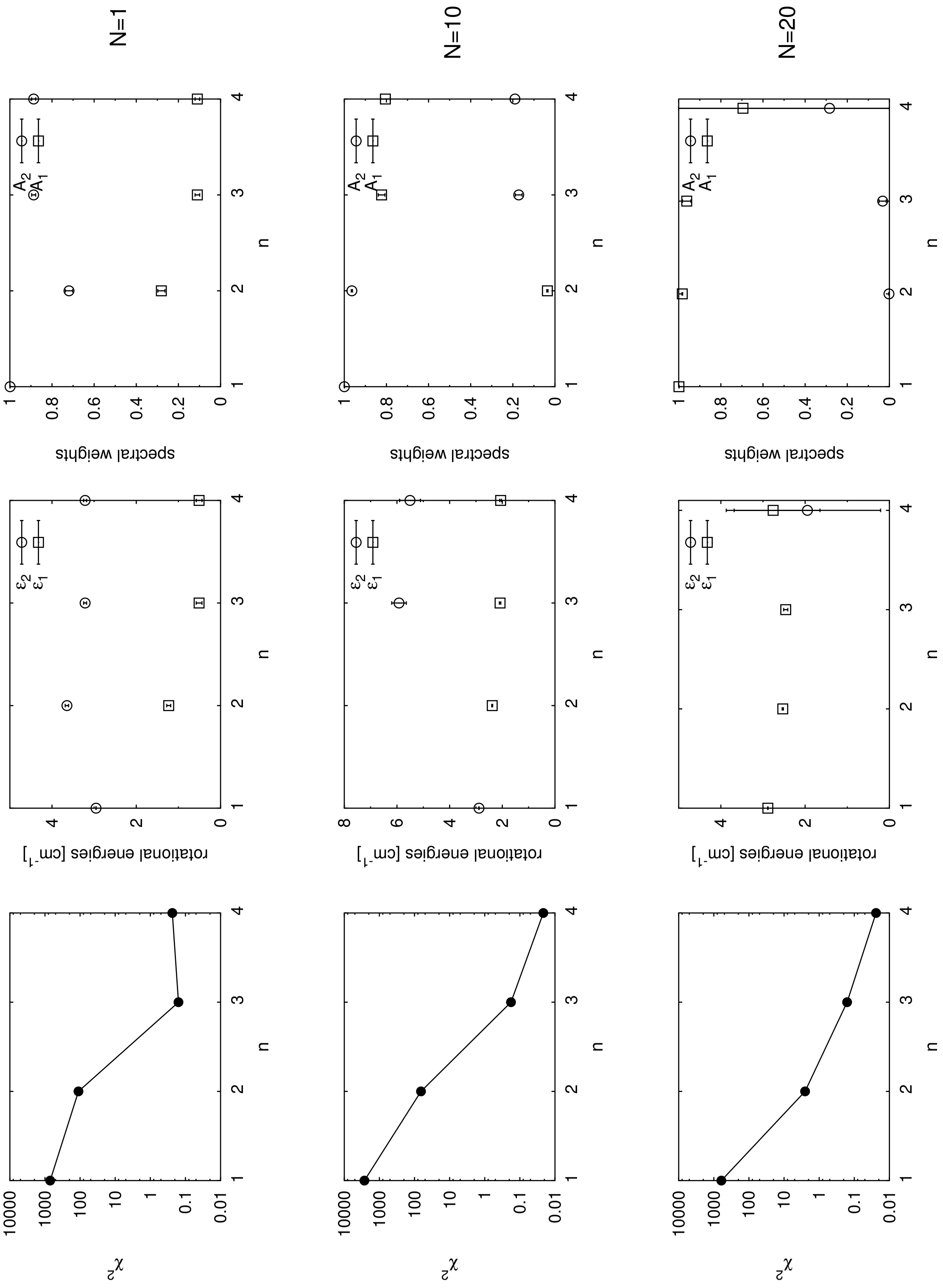

Figure 3.2: Comparison of three multiexponential fits for HCN@He$_N$. The three lines of graphs refer to the cases of $N = 1$, $N = 10$, and $N = 20$ respectively. The first column displays the χ^2 (solid circles) of the fit as a function of the number of exponentials, n, in Eq. 3.17. The other columns report the $J = 1 \leftarrow 0$ transition energies ε_i and the corresponding spectral weights A_i (indicated by the same symbols) as a function of n.

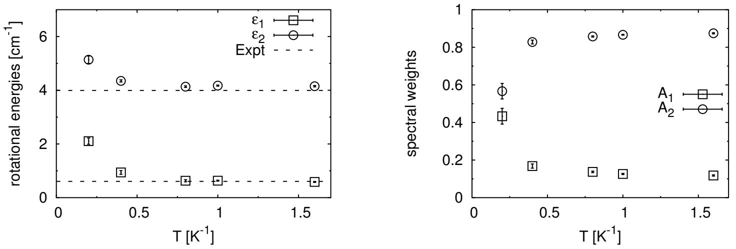

Figure 3.3: The two lowest rotational energies (left) and the corresponding spectral weights (right) for CO@He$_1$, extracted form the correlation function $c_{\hat{\mathbf{n}}}(\tau)$ for different length T of the internal portion on the path (see chapter 2). The dashed lines represent the experimental data of Ref. [5] for CO@He$_1$ referred to the center ν_0 of the vibrational band (see Sec. 1.2.2).

T. Full convergence of the results is achieved for $T = 0.8$ K^{-1} imaginary-time.

We finally remark that the use of Jackknife analysis [71] allows one to reduce the systematic bias affecting estimates of quantities which are a non-linear function of basic data (the time correlation functions in our case). In particular, for excitation energies and spectral weights, we first use the binning technique to eliminate autocorrelation on the basic data set, then we calculate the fluctuations of the fit parameters over the different data sets obtained by averaging all but one of the binning blocks.

3.5 Projection-time and time-step biases

The systematic errors coming from the finite projection time β and time step ϵ, can be removed by performing simulations at different time steps and projection times and extrapolating the results for $\epsilon \to 0$ and $\beta \to \infty$. In the left panel of Fig. 3.4 we report the estimated ground-state energy per particle, E_0/N, for a pure cluster of seven ^{4}He atoms, He$_7$, as a function of the time step, ϵ. The dependence of E_0/N on the time step is quadratic, as indicated by the best fit curve.

The right panel displays the energy per particle of He$_7$ as a function of β. For $\beta > 0.5$ K^{-1} most of the high energy components of the trial function have been filtered out and the energy has converged to its exact ground state value, within a

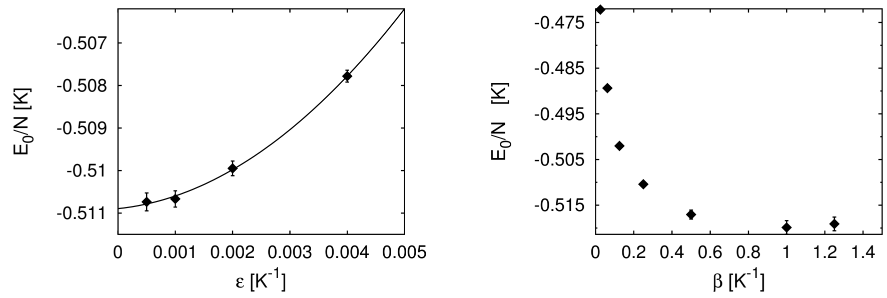

Figure 3.4: Left panel: energy per particle, E_0/N, in a pure cluster containing seven ^{4}He atoms (He$_7$), as a function of the time step ϵ. The black line represents the best fitting second order polynomial. Right panel: energy per particle of He$_7$, as a function of the projection time β. The time step is fixed at $\epsilon = 0.001\ \mathrm{K}^{-1}$.

few mK. For quantities like correlation functions, a more practical approach is to select a time step and a projection time such that the residual bias is smaller than the desired accuracy. In our simulations the total length $2\beta + T$ of imaginary-time paths is typically between one and two inverse Kelvin, with projections time between $0.1\ \mathrm{K}^{-1}$ and $0.4\ \mathrm{K}^{-1}$, and a time step $\epsilon = 10^{-3}\ \mathrm{K}^{-1}$.

3.6 Computational costs and path sampling

The CPU time per step increases quadratically with the number, N, of the helium atoms, due to the pair inter-particle potential, as well as to the trial function (for the largest simulated size, $N = 50$, one Monte Carlo step requires about 1 msec on a 1.4GHz PentiumIII). The global efficiency of the algorithm, however, has a less favorable scaling. Because of the global moves used in RQMC, the larger is the system, the lower is the acceptance rate (see *e.g.* the left panel of Fig. 3.5). As a consequence, the reversal of the slithering direction, accomplished by the bounce procedure, becomes more frequent, thus increasing significantly the average number of moves needed to refresh the whole path. This can be visualized in the right panel of Fig. 3.5, where we monitor the position of the head of the snake, $x(\tau)$, on the axis of the imaginary-time, for different sizes of HCN@He$_N$. We note that, to have a statistical error of $1.5 \times 10^{-2}\ \mathrm{cm}^{-1}$ on the lowest HCN@He$_N$

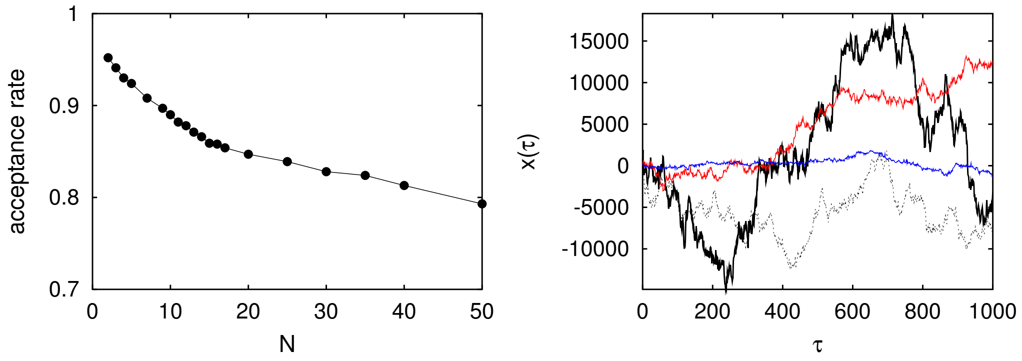

Figure 3.5: Left panel: acceptance rate for a He cluster doped with HCN, as a function of the size, N. In the simulations we employed a time step of 0.001 K^{-1}. Right panel: Diffusion $x(\tau)$ of the reptile head as a function of the random walk time τ, from RQMC simulation of HCN@He$_N$, for $N = 2$ (black solid line), 7 (black dotted line), 15 (red line) and 50 (blue line). The simulations have been performed with paths of 1000 time slices and time step $\epsilon = 0.001$ K^{-1}.

rotational energy, we need about 300 hours for $N = 15$ and $\sim$ 4900 hours for $N = 30$, on a 1.4GHz PentiumIII.

3.7 Toward the nanodroplet regime

For future work on larger clusters, we have implemented a different algorithm, the path integral ground state Monte Carlo [21, 61]. PIGS , as well as RQMC, relies on the path integral scheme for calculating ground state expectation values and imaginary-time correlations. The basic difference is in the sampling method. In PIGS the moves are performed by the *Bisection-Multilevel* (BSML) technique, used in state-of-the-art PIMC calculations [21, 47]. BSML uses multislices single-particle (or few-particles) moves, whose acceptance is largely independent of the system size. For an efficient implementation of PIGS, it is crucial to reduce the number of time slices as much as possible. This, in turn, requires to go beyond the primitive approximation for the propagator. Following Ref. [21], we adopt the pair action approximation, which allows accurate calculations for the condensed phase of helium, with a time step as large as 0.025 K^{-1}. We note that, at large sizes, the combination of such a time step with *global* moves results in a very low acceptance, thus limiting the effectiveness of the pair action in RQMC.

The pair action uses the exact expression of the propagator for a two-particle system to approximate the N-body propagator [21]. For spherical potentials, the former can be precomputed and tabulated, so that the full propagator can be evaluated quickly during the simulation [21] (see Appendix A).

When the interaction is anisotropic, such as the He-molecule one, a straightforward tabulation is not feasible. The standard choice [47, 72], in these situations, is to rewrite the anisotropic PES as a sum of spherical potentials plus a small correction, which are then treated in the pair and in the primitive approximation, respectively. We have applied this procedure to the He-CO interaction, as it is shown in the Appendix A. We note that for large time steps the Gaussian approximation of Eq. 3.3 for the rotations propagator, G_{rot}, has to be substituted with the exact expression (Eq. 3.2).

Now we discuss the efficiency of our PIGS implementation in the case of pure clusters. The efficiency of an algorithm, for a given property $\widehat{\mathcal{O}}$, can be defined as how quickly the error bars decrease as a function of the computer time [21]:

$$\xi_{\widehat{\mathcal{O}}} = \frac{1}{\sigma^2(\widehat{\mathcal{O}}) P T_{step}} \tag{3.18}$$

where $\sigma(\widehat{\mathcal{O}})$ is the statistical error on the Monte Carlo estimate of $\langle\widehat{\mathcal{O}}\rangle$, P is the number of steps of the simulation and T_{step} is the computer time per step.

In order to compare RQMC and our implementation of PIGS, we have evaluated the efficiency of the two algorithms for the calculation of the ground-state energy per particle, E_0/N, of a pure He cluster. The result is shown Fig. 3.6. In RQMC simulations the primitive approximation has been used with $\epsilon = 0.001\ \mathrm{K}^{-1}$. In the other case, thanks to the pair action, we could take a 25 times larger time step. The PIGS algorithm becomes more efficient than reptation for $N \gtrsim 100$. However, in the size range studied in this work ($N \leq 50$), RQMC is far superior than PIGS.

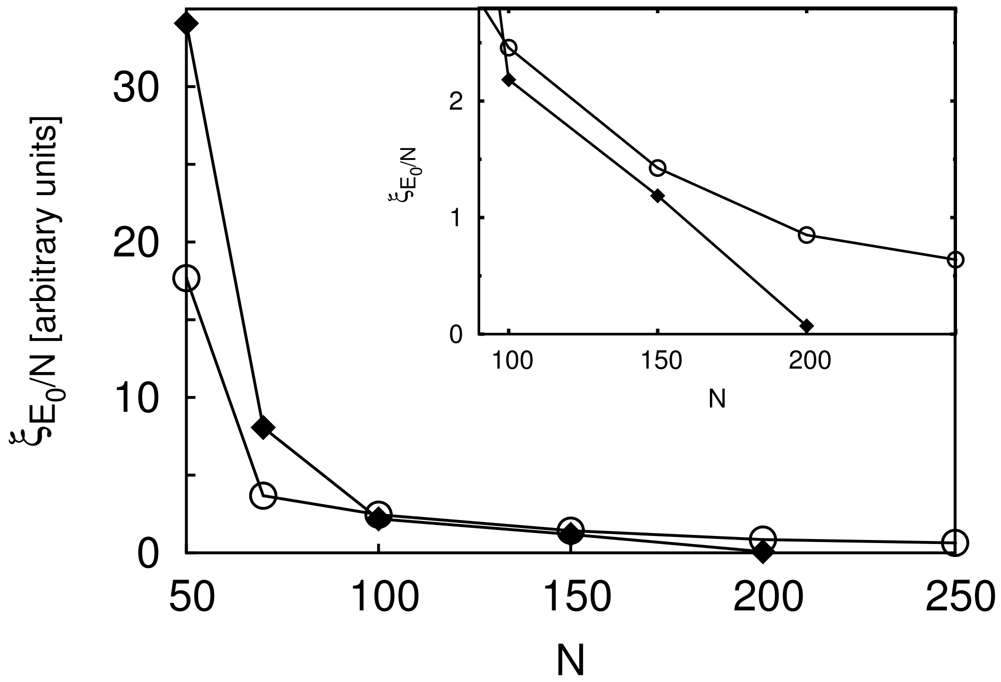

Figure 3.6: Efficiency in the calculation of the energy per particle, E_0/N, of He_N, as a function of the cluster size, N, for two different algorithms: RQMC (diamonds) and PIGS (circles). RQMC simulations have employed the primitive action with $\epsilon = 0.001\ \mathrm{K}^{-1}$. For PIGS (bisection-multilevel plus pair action) the time step was $0.025\ \mathrm{K}^{-1}$.

Chapter 4

Understanding the relation between structure and dynamics: CO@He$_N$

In this chapter, the rotational dynamics of CO@He$_N$ is studied using RQMC in the size range $N = 1-30$. We aim at elucidating the relation existing between the position, number, and intensity of the rotational lines and the size and structure of the cluster (see chapter 1). Our results reproduce rather accurately the roto-vibrational features of the observed CO@He$_N$ spectra [5], and allow for a detailed analysis of the interplay between structure and dynamics in these systems.

4.1 Ground state properties

RQMC simulations have been performed using the He-He and He-CO interactions of Refs. [64] and [20], respectively. Further technical details can be found in chapter 3. Fig. 4.1 shows the He-CO potential, $V(\mathbf{r})$, as calculated in Ref. [20], together with the atomic density distribution ρ_N, where ρ_N is the ground-state expectation value of the He density operator:

$$\widehat{\rho}(\mathbf{r}) = \sum_{i=1}^{N} \delta(\mathbf{r} - \mathbf{r}_i), \tag{4.1}$$

for a given cluster size, N. The He-CO PES, calculated in the ground state of the intra-molecular vibration, has one single shallow well of $V_m = -34.13$ K. This minimum is located on the oxygen side, at a distance of $r_m = 3.45$ Å from the

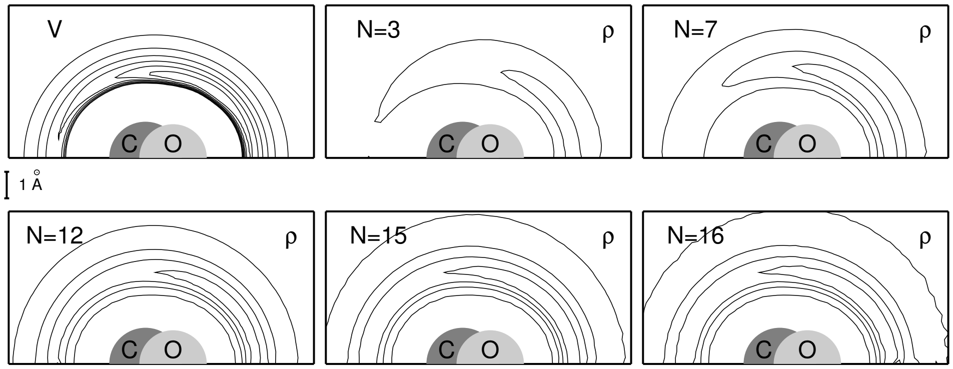

Figure 4.1: Upper left panel: He-CO interaction potential. C and O atoms are represented by two circles whose radius is the corresponding van der Waals radius. Contour levels start from $V = 0$ to negative values, and they are spaced by 5 K. The other panels depict the He density, ρ_N, for various sizes of the CO@He$_N$ cluster. For the density profiles, contour levels start from 0.001 with increments of 0.005, in unit of Å^{-3}. The lenght scale is indicated by the vertical segment corresponding to 1 Å.

CO center of mass, and at an angle $\theta_m = 48.8°$ from the molecular axis. For small N, the atoms start filling the potential well. As the number of He atoms increases the fluid overflows from the minimum and the borders of the dome stream down along the molecule. Already at $N = 4$ (not reported) some He density can be found all around the impurity, indicating that CO is fully solvated very rapidly. The most relevant aspect, shown by the density contour plots of Fig. 4.1, is the smooth evolution to an increasingly isotropic solvent distribution.

A more direct description of the solvation process is provided by a simultaneous analysis of the He atomic binding energy $\Delta E_N = E_{N-1} - E_N$ with the incremental atomic density distribution $\Delta\rho_N(\mathbf{r}) = \rho_N(\mathbf{r}) - \rho_{N-1}(\mathbf{r})$. The former quantity is reported in Fig. 4.2 as a function of the cluster size. ΔE_N first increases up to $N = 4 - 5$, and it stays roughly constant in the range $N = 5 - 8$; from this size on ΔE_N starts decreasing, first slowly, then, from $N = 10 - 11$, rapidly down to a minimum at $N = 19$. For $N > 19$ ΔE_N increases again and slowly tends to the nanodroplet regime (where it coincides with the bulk chemical potential, $\mu = 7.4$ K [18]) which is however attained for much larger cluster sizes than explored here [73].

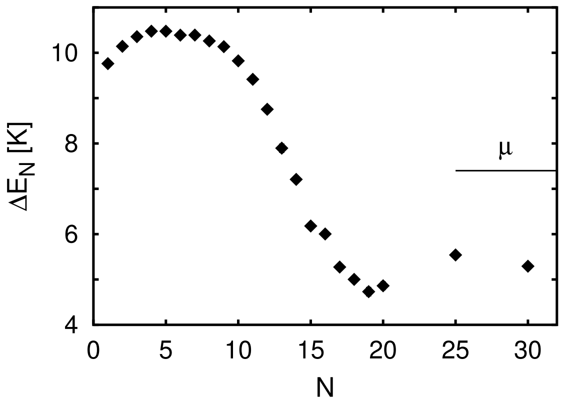

Figure 4.2: Atomic binding energy, $\Delta E_N = E_N - E_{N-1}$, as a function of the cluster size in CO@He$_N$. The horizontal line on the right of the figure indicates the chemical potential in bulk ^{4}He, $\mu = 7.4$ K [18].

This behavior can be understood by comparing $\Delta\rho_N(\mathbf{r})$ with the shape of the CO–He potential energy function, $V(\mathbf{r})$ (see Fig. 4.3). For very small N the atomic binding energy is dominated by the He–CO attraction of the potential well. As He atoms fill this well, ΔE_N first slightly increases, as a consequence of the attractive He–He interaction, then, for larger N, the increased He–He interaction is counter-balanced by the spill-out of He atoms off the main attractive well, until for $N \approx 9$ the reduction of the He–CO interaction overcomes the increased attraction and the binding energy starts decreasing steeply. For N in the range $10 - 14$, He atoms accumulate toward the C pole, while, around $N = 15$, the first solvation shell is completed and the differential atomic density, $\Delta\rho_N$, is considerably more diffuse starting from $N = 16$. ΔE_N reaches a minimum at $N = 19$. For larger sizes, the trend in the atomic binding energy is dominated by the increase of the He–He attraction related to the increase of the cluster size, until it converges to the bulk chemical potential.

4.2 Rotational spectrum

The energies of the two lowest rotational transitions $J = 1 \leftarrow 0$, $\epsilon^1_{a,b}$, as well as the corresponding spectral weights, $A^1_{a,b}$, are obtained form the imaginary-time

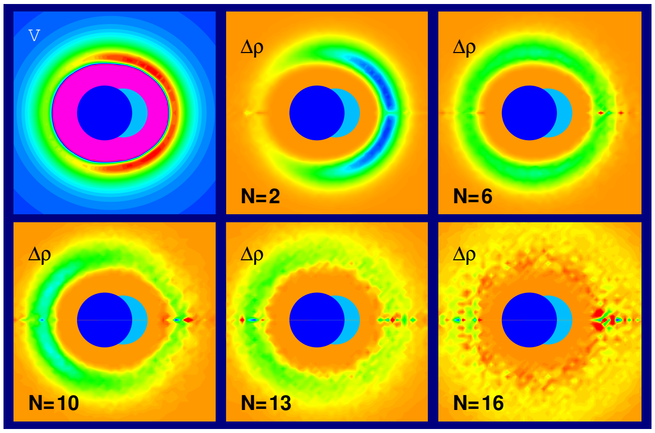

Figure 4.3: Upper left panel: He-CO interaction potential. C (blue) and O (cyan) atoms are pictured by two circles whose radius is the corresponding van der Waals radius. The other panels picture the differential He density, $\Delta\rho_N = \rho_N - \rho_{N-1}$ for various sizes of the CO@He$_N$ clusters. Color convention is rainbow: red to purple in order of increasing magnitude.

correlation function $c_{\hat{\mathbf{n}}}(\tau)$ with the procedure described in Sec. 3.4. In Fig. 4.4 we report the positions and spectral weights of the rotational lines, as functions of the cluster size, N. In the size range $N = 1 - 9$, analysis of the dipole time correlations clearly reveals the presence of two peaks, a-type and b-type, which correlate, respectively, with the end-over-end rotation and with the free molecule rotation in the He-CO complex (see Sec. 1.2.2). The spectral weights of the b-type series rapidly decrease by almost a factor 2. Note that the sum of the spectral weights of these two lines nicely sums to one, indicating that they exhaust all the oscillator strength available for optical transitions originating from the ground state. For N between 10 and 12 (shaded area in Fig. 4.4) the situation is less clear. As the weight of the b-type line drops to zero, the statistical noise on its position grows enormously. Furthermore the multi-exponential fit introduces some ambiguity, as the results become somewhat sensitive to the number of terms in the sum. However the important information that one line disappears between $N = 10$ and 12 is clear. For larger N only one relevant line remains, and the robustness of the fitting procedure is recovered, with the minor exception of the sizes around $N = 16$, where the minimum of the χ^2 appears to be less sharp, possibly correlating with

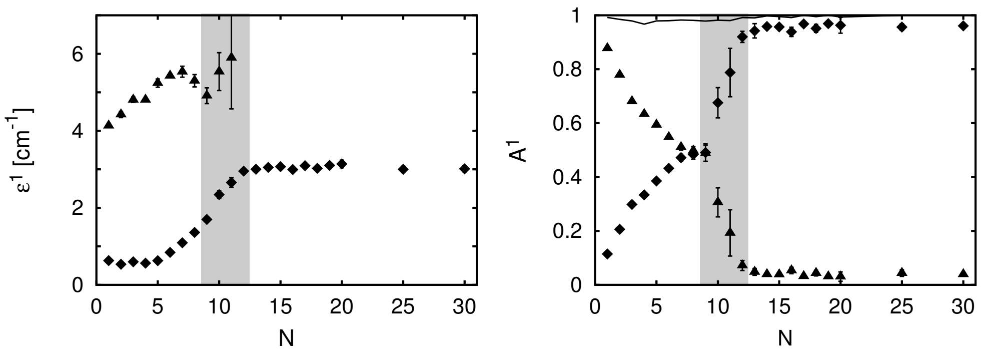

Figure 4.4: Left panel: position of the rotational lines of CO@He$_N$ as obtained from RQMC simulations as a function of the cluster size, N. a-type lines are indicated with diamonds, b-type lines with triangles. Right panel: spectral weights of the lines reported in the left panel; the continuous line near the upper border of the figure corresponds to the sum of the spectral weights.

the splitting of the line observed in the infrared spectra for $N = 15$ (see below). The surviving series of transitions shows no dependence on N, thus indicating the onset of a nearly free rotation regime.

In the left panel of Fig. 4.5 we compare the rotational structure of the observed infrared (vibrational) spectrum [5] with the rotational excitation energies that we have calculated. Experimental data are referred to the center, ν_0, of the vibrational band for $N = 0$ (CO monomer). In order to better compare our predictions with experiments, we have corrected the former with an estimate of the vibrational shift $\Delta\nu_0$ (the displacement of the vibrational band origin as a function of the number of He atoms, see Sec. 1.2.2). The vibrational shift can be calculated as the difference in the total energy of the cluster obtained with two slightly different potentials [20], V_{00} and V_{11}, representing the interaction of a He atom with the CO molecule in its vibrational ground state and first excited state, respectively [32]. Since the evaluation of a small difference between two large energies is computationally demanding for large clusters, $\Delta\nu_0$ has been evaluated perturbatively with respect to the difference $V_{00} - V_{11}$ using a correlated sampling technique [73]. We have used the vibrational shift calculated in Ref. [73] after verifying on small clusters that the perturbative treatment is reliable.

The good agreement between theory and observation is quite evident, and contributes to validate the procedure used to extract the rotational energies from

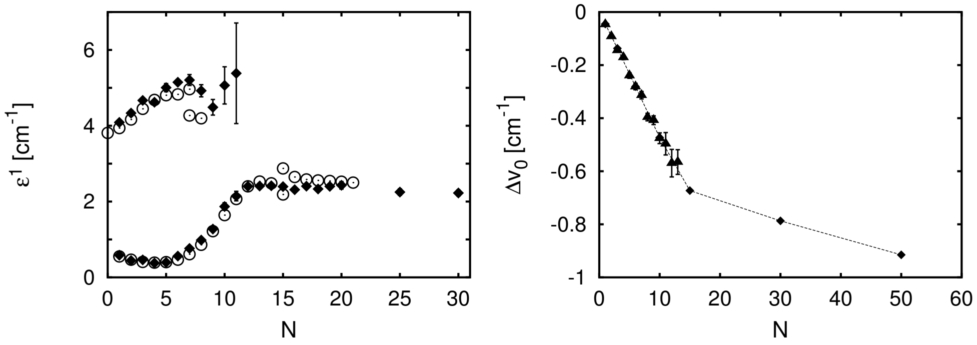

Figure 4.5: Left panel: positions of the infrared lines of CO@He$_N$ as observed experimentally (Ref. [5], empty circles) and as estimated from the present simulations and corrected by the estimated vibrational shift (solid diamonds, see text). Right panel: vibrational shift of the lines, as estimated in the present work (triangles) and in Ref. [73] (diamonds and dashed line).

imaginary-time correlation functions. We stress that the analysis of the dipole correlation function, is able to disclose both the presence of two lines in the spectrum and the fading of the b-type one. The behavior of the corresponding estimated spectral weights (see Fig. 4.5) shows that the higher frequency series does not disappear abruptly, but gradually looses intensity in favor of the a-type one. The spectral weights indicate a smooth transition between two dynamical regimes, suggesting that, with increasing the size, slow changes are occurring in CO@He$_N$.

4.3 Structure and dynamics

Despite the remarkable agreement between our results and experiments, some of the features of the observed spectrum call for a deeper understanding and theoretical investigation. Two questions, in particular, naturally arise. Why are two peaks observed in the small-size regime, and what does determine the disappearance of one of them at $N = 8$? What does determine the split of the higher-frequency (b-type) line at $N = 7$ and of the lower-frequency (a-type) one at $N = 15$?

The existence of two lines for small N is likely due to a larger asymmetry of the cluster in this regime. If the CO@He$_N$ complex is described as a rigid rotor, in fact, one would have one rotational line originating from a $J = 0$ ground state if the complex has cylindrical symmetry, while this line would double if some of the atomic density accumulates in a longitudinal protrusion. The inertia of the complex would in this case be larger for a rotation about an axis perpendicular to a plane containing the protrusion (*end-over-end rotation*) than about an axis lying on such a plane. Given that the Hamiltonian of the system is invariant under rotation about the molecular axis, any breaking of this symmetry can not be revealed by the ground state He atomic density. In Fig. 4.1, no difference can be found in the reported contour plots, although they correspond to extremely different dynamical situations: at $N = 3$ the spectrum consists of two transitions; at $N = 7$ the b-type line splits and the a-type one is still present. $N = 12$ is exactly the size at which the higher energy line disappears. Finally, no significant change appears between the solvent densities of CO@He$_{15}$ and CO@He$_{16}$. Nevertheless, in the former case a doubling of the a-type line is observed, while in the latter the nearly free rotation regime is restored.

In order to detect a possible asymmetric structure, we need a correlation function of higher order than the density. Hence, we define an atomic angular correlation function, $C(\phi)$, as the probability of finding two He atoms which form a dihedral angle ϕ with respect to the molecular axis:

$$C(\phi) = \left\langle \frac{1}{N(N-1)} \sum_{i \neq j} \delta(\phi_i - \phi_j - \phi) \right\rangle . \tag{4.2}$$

In the left panel of Fig. 4.6 we show $C(\phi)$, for different cluster sizes. The depletion of C for ϕ larger than $\pi/2$, clearly visible for $N = 3$ (green circles), indicates a tendency of the He atoms to cluster on a same side of the molecular axis. For larger clusters this effect weakens, suggesting the approach to the cylindric distribution. However, the larger is the cluster size, the harder is the distinction of the signal of an asymmetry from the structural information related to the He–He interaction. As N increases, the features of $C(\phi)$ tend to resemble those of the liquid He radial pair distribution: the dimple due to steric repulsion, the nearest-neighbor peak and the subsequent plateau. Once the latter has appeared in $C(\phi)$, it is difficult to interpret the maximum around $\phi = 0.3 - 0.4\,\pi$ as a clear proof of an asymmetric arrangement of the He density.

A more sensitive measure of the propensity of He atoms to cluster on a side of

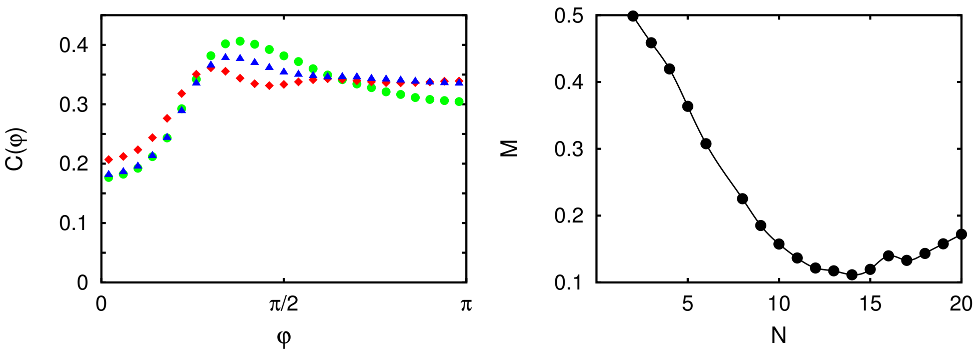

Figure 4.6: Left panel: probability density of finding two He atoms which form a dihedral angle ϕ with respect to the molecular axis; the probability is normalized to 1. Results pertain to clusters with $N = 3$ (green circles), $N = 6$ (blue triangles) and $N = 13$ (red diamonds). Right panel: The integrated probability density, defined in Eq. (4.3), as a function of the cluster size.

the molecule is given by the integral of $C(\phi)$ from 0 to $\frac{\pi}{2}$,

$$M = \int_0^{\frac{\pi}{2}} C(\phi) d\phi - \frac{1}{2}. \tag{4.3}$$

M measures the deviation of the He density distribution from the cylindrical symmetry. In the right panel of Fig. 4.6 we display M as a function of the cluster size, N: one sees that M decreases with N and reaches a minimum at $N = 14$. This is precisely the size at which the first solvation shell is completed and thus, for steric reasons, the He atomic distribution is more homogeneous. The cluster asymmetry increases again when the second shell starts to build. The rotational spectrum of the solvated molecule, however, is insensitive to this asymmetry for clusters of this and larger sizes. This indicates that the existence of the asymmetry is a necessary but not sufficient condition for the line doubling. If quantum fluctuations make the motion of the protrusion fast with respect to the molecular rotation, the impurity perceives a cylindrical effective distribution. The existence of two lines in the rotational spectrum of the molecule requires therefore that an asymmetry in the *instantaneous* distribution of He atoms around the molecular axis exists; that the molecular inertia is sensitive to this asymmetry (the protrusion can be 'dragged' along the molecular rotation); and that the motion of this protrusion around the molecular axis is slow enough with respect to the molecular rotation.

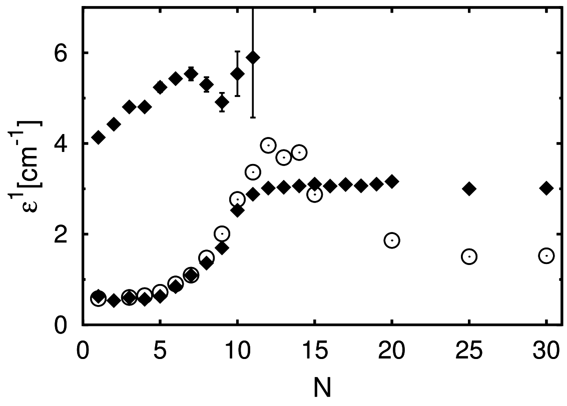

Figure 4.7: Diamonds: CO rotational frequencies in CO@He$_N$ as functions of the cluster size, N (same as in Fig. 4.4). Dots: frequency of the lowest mode appearing in the spectral analysis of the angular He–He correlation function (see Eq. (4.4)).

In order to better characterize the motion of He atoms around the molecule and their coupling to the molecular rotation, we examine the imaginary-time correlations of the versor, $\mathbf{u}$, of the He center of mass, $\mathbf{r}_{CM}$, relative to the molecular center of mass:

$$\mathcal{C}_{\mathbf{u}}(\tau) = \langle \mathbf{u}(\tau) \cdot \mathbf{u}(0) \rangle. \tag{4.4}$$

For the binary complex, He–CO, $\mathbf{r}_{CM}$ coincides with the position of the helium atom, and we expect its angular dynamics to be strongly correlated to the molecular rotation, at least in the end-over-end mode. In Fig. 4.7 we report the frequency of the slowest mode appearing in the spectral analysis of $\mathcal{C}_{\mathbf{u}}(\tau)$, $\epsilon_{\mathbf{u}}$, as a function of N, and compare it with the corresponding frequencies of the molecular rotation. We see that for cluster sizes up to $N = 9 - 10$, $\epsilon_{\mathbf{u}}$ is degenerate with the a-type frequency in the molecular rotational spectrum, with a spectral weight which passes from $A_{\mathbf{u}} \approx 1$ for $N = 1$ to $A_{\mathbf{u}} \approx 0.7$ for $N = 10$. These findings are a manifestation of the fact that He atoms are dragged along the slowest, end-over-end, rotation of the solvated molecule, and that the effect of this dragging decreases when more He states with $J = 1$ become available and subtract spectral weight to the slowest mode. For $N > 10$, $\epsilon_{\mathbf{u}}$ further increases and departs from ϵ_a, indicating an effective decoupling of the two kinds of motion. The lowest atomic mode, $\epsilon_{\mathbf{u}}$, slows down again for $N = 15$. This is due, however to the slow He motion in the second solvation shell which hardly affects the rotation of the solvated molecule. Although the resolution that can be achieved with our simulations is not sufficient to detect the doubling of the a and b lines which is experimentally observed for $N = 15$ and $N = 7$ respectively, it is interesting to notice that the former occurs in correspondence with the crossing between $\epsilon_{\mathbf{u}}$ and ϵ_a, possibly due to the resonant interaction between the two modes. It is tempting to assume that a similar mechanism may be responsible for the doubling of the b line at $N = 7$, involving however higher-energy He states. A deeper study of the He dynamics would clarify this point.

In a recent theoretical work [66] the onset of the nearly free rotation regime ($12 \lesssim N \lesssim 20$) is connected to the b-type line, as it would be expected from the notion of b-type mode in the He-CO dimer. Here we propose a different view, in which the free rotation series simply evolves from the a-type one when the latter departs from the series of the He mode. We add that, when the cluster size increases, it looks inappropriate to distinguish the two kinds of spectral lines by resorting to the concepts of a- and b-type lines as defined for the dimer. This conclusion was already suggested by the authors of Ref. [5].

4.4 Summary and discussion

Using RQMC, the CO dipole autocorrelation function has been calculated, allowing to reproduce rather accurately the rotational features in the IR spectrum of CO@He$_N$ [5]. The presence of two spectral lines—a-type and b-type, evolving respectively from the end-over-end and from the free-molecule rotations of the binary complex—is revealed and related to the propensity of the He atoms to cluster on a same side of the molecular axis. This propensity is measured by an appropriate angular pair distribution function. We find that as more He atoms progressively fill the first solvation shell, their clustering propensity weakens; the CO impurity gets more isotropically coated, looses a preferred axis for the free-molecule mode, and the b–type line disappears.

Additionally, dynamical information on the He atoms in excited states with $J = 1$ has been obtained, by calculating the time autocorrelation of the versor of the He center of mass. We find a substantial spectral weight on a He mode whose energy, $\epsilon_{\mathbf{u}}$, is degenerate with the a-type line for N up to about ten. This indicates that some of the He density is dragged along by the molecular rotation—in other words, part of the angular momentum in the cluster mode involving molecular rotation is carried by the He atoms. We also find that for larger clusters the molecular rotation effectively decouples from this He mode, and its energy ϵ_a becomes essentially independent of the number of He atoms. We relate the onset of the free-rotor-like regime and the evolution of the a-type series. When the cluster size approaches the critical value of $N = 12$, it is no more possible to think of the a- and b-type transitions as they are meant for the binary complex.

Extrapolating the result obtained for N up to 30 to the nanodroplet limit, we have predicted a renormalization factor of the B value of 0.78. A recent experiment [57], however, indicates that in large droplets the effective B is 63% of the gas phase value. In Ref. [57] these findings have been rationalized in terms of coupling between phonon modes of the solvent and molecular rotation. Our calculations do not allow us to draw any conclusion on this problem, but we consider it a target for further studies.

Our results show how computer simulations of small molecules solvated in He clusters can provide direct information on the dynamical processes observed in spectroscopic investigations. Rotational lines are predicted with high accuracy. Even more importantly, computer simulations give access to quantities (such as, e.g., binding energies, density distribution, dynamics of the He matrix) not directly accessible by the experiments, but whose knowledge allows for a deeper understanding of the relations between structure and dynamics in these confined boson systems.

Chapter 5

Toward the nanodroplet regime

In this chapter we focus on the effective rotational constant of He solvated rotors, addressing the problem of its convergence to the nanodroplet limit and of its reduction upon solvation. In particular, we want to understand the relative importance of the bare molecular inertia and of the anisotropy of the He-molecule in determining the rotational properties of solvated molecules. Hence, using RQMC, we have first simulated OCS@He$_N$ and HCN@He$_N$, chosen as paradigmatic cases of heavy and light solvated molecular rotors, respectively. Then, we have performed computer experiments in which the rotational dynamics of OCS and HCN molecules was simulated using a fictitious inertia appropriate to the *other* molecule. Our findings indicate that the approach to the nanodroplet regime, as well as the reduction of the molecular inertia upon solvation, is determined by the anisotropy of the potential, more than by the molecular weight. Our conclusions are positively supported by the remarkable agreement with the available experimental data, and also by the results of the previous chapter.

5.1 Molecule-atom interactions

For both OCS@He$_N$ and HCN@He$_N$, the He-He and the He-molecule interactions are parametrized after accurate ab-initio quantum chemistry calculations [33, 64, 65]. For the He-OCS PES, in particular, we use the *unmorphed* version of Ref. [33]. In the next section we show that this version—which results from a direct fit to quantum-chemistry calculations—is considerably more accurate for a

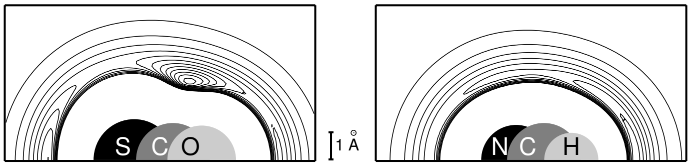

Figure 5.1: Potential energy surfaces of He-OCS (left) and He-HCN (right) used in this work. The He-OCS PES is the *unmorphed* version from Ref. [33] (see text). The length scale is indicated by the vertical segment corresponding to 1 Å. Contour levels start from $V = 0$ to negative values, and they are spaced by 5 K.

wide range of cluster sizes [74] than the *morphed* one which was refined so as to improve the predictions for the spectrum of the OCS@He$_1$ complex [33]. Contour plots of the He-HCN and the He-OCS PES are displayed in Fig.5.1, showing a much greater strength and anisotropy of the latter.

The He-OCS interaction potential has a deep *equatorial* doughnut-shaped well around the C atom, and two secondary *polar* minima in correspondence of the O and S atoms. The OC an CS bond lengths are fixed at 1.16 Å and 1.56 Å respectively. The global minimum is $V_m = -62.26$ K deep and it is located at $R_m = 3.40$ Å from the OCS center-of-mass, at an angle $\theta_m = 69.7°$ with respect to the molecular axis. The well at the oxygen side has a dept of -36.27 K and it is 4.82 Å away from the OCS center-of-mass. At 4.52 Å from the latter, near the sulphur, the potential energy surface reaches -40.14 K, forming a deeper and broader well than at the oxygen end. The two linear minima are separated from the global one by transition states found at $(R/\text{ Å}, \theta/°) = (4.33, 119.1)$ and $(4.55, 29.4)$, with energies -22.75 K and -34.30 K. Hence the potential in the region of the oxygen atom is quite flat.

The He-HCN interaction, instead, has a shallow main minimum of -43.02 K, in correspondence with the hydrogen molecular pole. The bottom of the main well is located at 4.22Å from the molecular center of mass. A secondary minimum appears slightly below the equator on the nitrogen side, at a bent geometry. This shallower well is situated at 3.59Å from the HCN center-of-mass, at an angle $108.5°$, and has a depth of -31.75 K. The region of the PES in the vicinity of the local minimum is very flat, and the latter is barely visible in the lower panel of

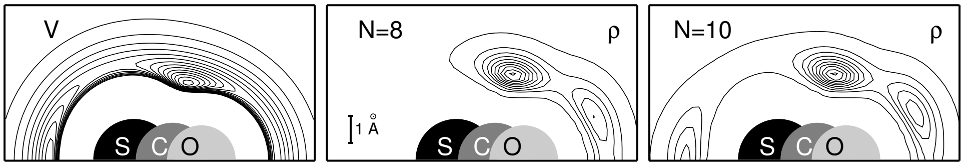

Figure 5.2: Left panel: potential energy surface of He-OCS (we display here the *morphed* version from Ref. [33] which was used in Ref. [18]). Right panels: contour plots of the helium density profiles of OCS@He_8 and OCS@He_{10}. The length scale is indicated by the vertical segment corresponding to 1 Å. For the density profiles, contour levels start from 0.001 with increments of 0.005, in units of $Å^{-3}$.

Fig. 5.1. The HC and CN bond lengths are considered fixed at 1.07Å and 1.15Å.

5.2 Carbonyl sulfide

5.2.1 Appraising the quality of intermolecular potentials

After the experiment of Jäger *et al.* [4], the rotational dynamics of OCS@He_N in the small and intermediate size range, has been addressed by several theoretical studies [13, 31, 55], in which variable agreement with experimental data was found.

Much of the discrepancy between the results of quantum Monte Carlo simulations and experiments (as well as *among* different simulations, we should add) may be due to the quality of the He-molecule potential utilized for the simulations [31]. In Ref. [55] it was in fact shown that the difference between the predictions of Refs. [31] and [13] is indeed (almost) entirely due to the poorer quality of the potential utilized in Ref. [13]. In Fig. 5.2 we compare the atomic density distributions of OCS@He_8 and OCS@He_{10} with the He-OCS potential used in Ref. [31]. According to the analysis of Ref. [31], the minimum in the effective inertia of the solvated OCS molecule occurs at the largest cluster size at which quantum tunneling between the main, *equatorial*, and the two secondary, *polar*, potential wells is hindered by the energy barriers which separate them. It is clear that the larger the barrier, the smaller the tunneling, and the larger the corresponding effective inertia will be. In Ref. [31] it was indeed found that fudging the He-OCS PES—so as to enhance the potential energy barrier which separates the main well from the molecular poles—hardly affects the rotational constant for $N \leq 5$, while it increases the inertia for $N = 6, 7, 8$, thus bringing the results of the simulations in much better agreement with experiments. It was later found that this too low a value for the relevant energy barriers is in fact an artifact of the *morphing* procedure adopted in Ref. [33], where an already very accurate OCS-He potential obtained from coupled-cluster quantum-chemical calculations has been morphed to yield an even better agreement with the known spectra of the OCS@He$_1$ complex. As a consequence of the morphing, the transition state near the oxygen end is made 2.06 K deeper, so that the PES becomes even flatter between the global minimum and the O pole. The lower barrier favours quantum tunneling, thus producing, for $N \geq 5$, the fictitious decrease of the OCS@He$_N$ effective inertia calculated in Ref. [31].

We conclude that the spectra of clusters with many He atoms—which depend on the PES far from the minimum—are a much more sensible benchmark of the overall quality of the PES than those of the helium-molecule dimer. A similar conclusion was drawn in Ref. [55] where a different He-OCS PES was proposed, such that the rotational constants calculated from POITSE simulations agree well with experimental data available for $N \leq 8$. RQMC simulations performed with this PES in the size range $10 \leq N \leq 30$ show a behavior of the rotational constant very similar to that reported in Fig. 5.4, obtained from the *unmorphed* version of the PES of Ref. [33], although the resulting values are slightly smaller for the largest sizes (hence closer to the experimental nanodroplet regime: see below).

5.2.2 Solvent density

Fig. 5.3 displays the He density profiles of OCS@He$_N$, at various sizes. For $N = 1 - 5$, the solvent fills the main equatorial well of the potential, forming a ring around the molecule. With the sixth atom the density in the ring keeps increasing, although slightly, but the main effect is its spill over into the shallow well at the oxygen side. The overflow of the Helium toward the O end continues with up $N = 8$, even if the sulphur minimum is deeper. This is so because the potential barrier between the global minimum and the oxygen pole is lower than toward the opposite hemisphere. At $N = 10$, the He density has reached the

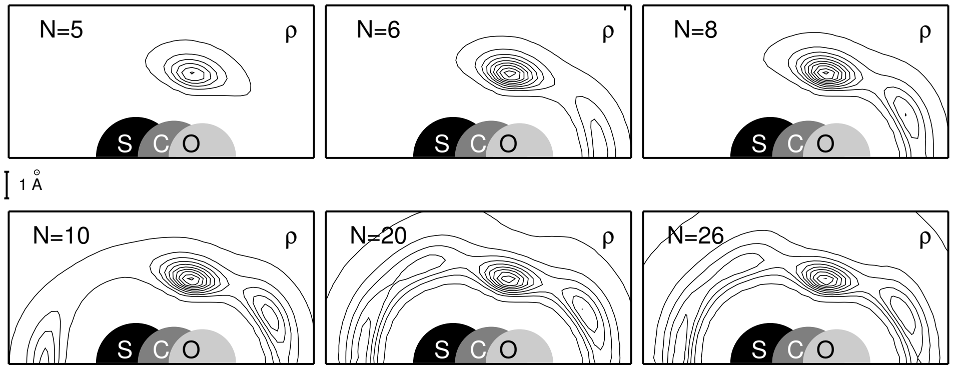

Figure 5.3: He density, ρ_N for various sizes of the OCS@He$_N$ cluster. Contour levels start from 0.001 with increments of 0.005, in unit of Å^{-3}. The length scale is indicated by the vertical segment corresponding to 1 Å.

S end and the dopant impurity is fully coated by the solvent. The implications of this full solvation on the rotational dynamics of the molecule are discussed in the next section. Between $N = 20$ and $N = 26$ no significant changes occur in the He distribution of the inner region of the cluster. We can thus infer that at $N = 20$ a first shell of solvation has been completed. It can be noticed that, starting from $N = 6$ the density maximum in the equatorial ring is not modified by the further addition of He atoms. At the same time, the other local structures in the inner shell persist and the density maintains an highly anisotropic shape up to the largest simulated clusters.

5.2.3 Effective rotational constants

In Fig. 5.4 we report the dependence of the effective rotational constant, B, on the cluster size, N, as calculated with the unmorphed He-OCS potential of Ref. [33]. The nanodroplet limit resulting from measurements on clusters of ≈ 6000 atoms [3] is indicated by a dashed line. RQMC results compare favorably with experimental data which are available up to $N = 8$ [4]. In the small-size regime ($N \leq 8$) the rotational constant decreases with increasing cluster size because the He atoms trapped in the (*equatorial*) and in the first *polar* (near oxygen) well are dragged along by the molecular rotation, thus increasing the effective inertia. For $N > 8$—

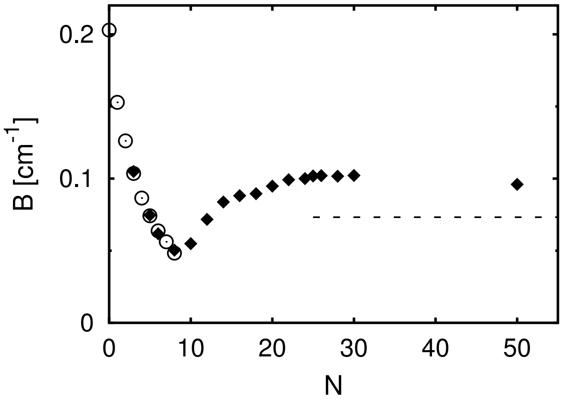

Figure 5.4: Effective rotational constant of OCS@He$_N$, as a function of the cluster size, N. Diamonds: results from RQMC simulations performed using the unmorphed potential of Ref. [33] (see text). Open circles: experimental data from Ref. [4]. The horizontal dashed line indicates the nanodroplet limit measured in Ref. [3].

as the second *polar* (near sulphur) well starts to be filled—an increasing fraction of the He atoms can freely tunnel among different wells, thus not contributing to the molecular inertia. The quantum fluid nature of the He solvent is such that tunneling is a collective process in which not only the excess atoms not fitting in the main potential well take part, but even those which are tightly bound to it. For this reason, once tunneling among different wells is made possible by the spill-out of excess atoms, this process determines a decrease of the molecular inertia, *i.e.* an increase of the rotational constant for an increasing cluster size. As a matter of fact, it was shown in Ref. [31] that the value of the correlation between the molecular angular momentum and the atomic angular current—which is maximum in the main *equatorial* potential well—starts decreasing as the rotational constant increases past the minimum ($N > 8$). This decrease continues until the first solvation shell is completed at a cluster size $N \approx 20$, around which the rotational constant seems to stabilize. As the second solvation shell starts to build, however, quantum exchange cycles involving atoms from this shell would contribute to further, although weakly, decrease the molecular inertia. A similar behavior of the evolution of the rotational constant for sizes shortly beyond completion of the first shell is also observed in simulations of clusters doped with N_2O and

CO_2 [16, 34], which are all molecules having a qualitatively similar interaction with He atoms. Our findings demonstrate that—contrary to a commonly accepted assumption [2]—He atoms from outer (larger than the first) solvation shells do affect the molecular inertia. For N_2O and CO_2 this is also supported by experimental evidence [6, 7]: the measured value of B for the largest cluster with secure assignment of spectral lines ($N = 12$ for N_2O and $N = 17$ for CO_2) is significantly higher than the nanodroplet limit, with no plausible signs of convergence within the first shell. A role of outer shells in bringing down the effective rotational constant is thus to be expected. How far from the molecule does this effect extend, our simulations—which are limited at present to a few tens atoms—cannot say yet. This finding is at least compatible with current phenomenological models of the inertia of He-solvated molecules, which predict a lower contribution of the solvent to the molecular inertia, with decreasing atomic density. In hydro-dynamical models [9, 10] a lower atomic density would determine a reduced kinetic energy of the irrotational flow of the solvent; in a two-fluid model [46], instead, a lower inertia would simply follow from a reduction of the nonsuperfluid component of the atomic density. Coming down from the nanodroplet regime, a decrease of the atomic density in the first solvation shell(s) is indeed expected, as a consequence of the reduced pressure exerted by the outer shells. This is clearly demonstrated in Fig. 5.5 in which the He radial density profiles around OCS are compared for $N = 20$ and $N = 50$. The radial density in the first shell is significantly lower for the smaller cluster. On purely classical grounds, a competing effect could arise if the spatial extension of the first shell was sensitive to the pressure release, thus affecting the second moments of the atomic density. The density profiles shown in Fig.5.5, however, suggest that this effect is small, since the positions of the peaks in the first shell hardly change between clusters of 20 and 50 He atoms.

Our results demonstrate that in OCS@He_N clusters the effective rotational constant does not attain its asymptotic limit upon completion of the first solvation shell, being in fact higher at this size. When the second shell starts to build up, the value of B further increases (arguably, via quantum exchange cycles involving particles of both shells [34, 47]). Whether, in larger clusters, the missing inertia will be recovered by a change in the density of the first shell or by a direct contribution from the outer shells, or both, remains to be investigated.

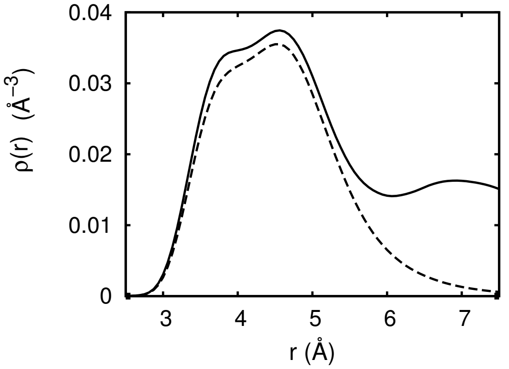

Figure 5.5: Radial density profile $\rho(r)$ of He in OCS@He$_N$ for $N = 20$ (dashed line) and $N = 50$ (solid line).

5.3 Hydrogen cyanide

Hydrogen cyanide (HCN) is considered to be a prototype of light helium-solvated rotors [2, 11], for which the assumption of *adiabatic following* breaks down. This has been demonstrated both experimentally, by comparing the rotational constants of HCN and DCN in the nanodroplet regime [50], and theoretically, by comparing the He density profiles obtained from simulations performed including and, in turn, neglecting the molecular degrees of freedom [14]. The calculation of the molecular rotational constant, B, in large droplets thus defies the application of either the two-fluid [11] or hydrodynamic [9] models, which both rely on the concept of *adiabatic following*, albeit in a different manner (see Sec.1.3). On the other hand, direct calculations of rotational excitations by the POITSE method [14] indicated that the nanodroplet value would not be reached even for $N = 25$, well beyond completion of the first solvation shell. This slow convergence of the rotational constant as a function of the cluster size was later attributed to the coupling of molecular rotation to phonon-like excitations of the solvent which would develop only in the nanodroplet regime [15]. Unfortunately experimental data for the effective rotational constant of HCN are only available, so far, for very large droplets [50]. We will see however how a comparison of our theoretical results for HCH@He$_N$ with both theoretical and experimental results which are available for the closely related CO@He$_N$ system will allow to draw a number of important and non trivial conclusions.

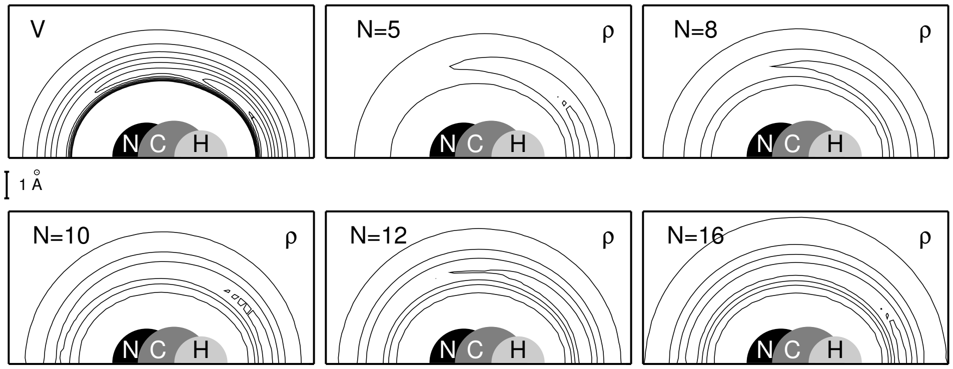

Figure 5.6: Upper left panel: He-HCN interaction potential, the same as in Fig.5.1. The other panels depict the He density, ρ_N for various sizes of the HCN@He$_N$ cluster. For the density profiles, contour levels start from 0.001 with increments of 0.005, in unit of Å^{-3}. The length scale is indicated by the vertical segment corresponding to 1 Å.

5.3.1 Structural properties

In Fig. 5.6 we display the He-HCN potential—already reported in Fig.5.1—along with the He atomic density distributions at different sizes. The contour plots evidence how the solvent forms, at first, a broad cap around the H end of the HCN molecule, centered on the main potential well of the PES. With increasing N, the He atoms flow out of the minimum and surround the impurity. By comparing the density profiles of HCN@He$_N$ with those of OCS@He$_N$, we note that the solvent distribution is much less structured in the former case, as expected from the more isotropic He-molecule interaction. A careful consideration of the PES can also explain the slight differences between the density profiles of CO@He$_N$ with respect to HCN@He$_N$. The pictures of Fig. 4.1 and Fig. 5.6 corresponding to the same sizes show that the He distribution around CO has a maximum as high as in HCN@He$_N$. Nevertheless, in the latter system, the density peak is slightly thinner and more stretched toward the opposite pole. In other words, as N increases, the solvent spills out of the potential minimum and streams down along the molecule more rapidly in HCN@He$_N$ than in CO@He$_N$. This effect can be related to the amplitude of the wells of the PES. In the case of the He-HCN interaction the narrower well can contain a smaller amount of solvent than the minimum of the

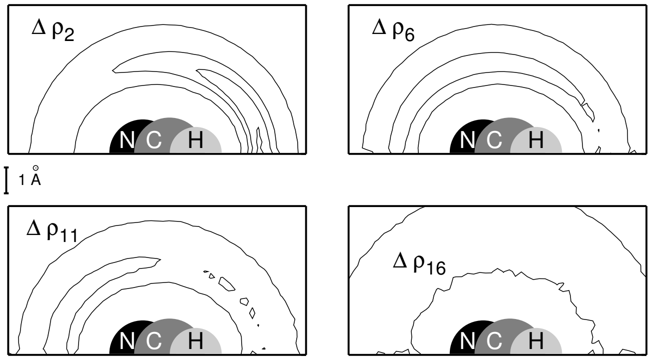

Figure 5.7: Contour plot of the incremental density, $\Delta\rho_N(\mathbf{r}) = \rho_N(\mathbf{r}) - \rho_{N-1}(\mathbf{r})$, for selected HCN@He$_N$ clusters. The HCN molecule has its center of mass at the origin, with the hydrogen atom on the positive z direction. The length scale is indicated by the vertical segment corresponding to 1 Å. Contour levels start from 0.0001 with increments of 0.001, in units of inverse cubic Å.

He-CO PES. The latter is thus filled slowly and the density peak is therefore less dispersed. In spite of these differences, CO@He$_N$ and HCN@He$_N$ are similar among them, and much more isotropic than OCS@He$_N$.

In order to better characterize the solvation process of HCN@He$_N$ and, moreover, to evidence the strong analogy with the case of CO@He$_N$, we analyze the incremental atomic density profile of HCN, $\Delta\rho_N(\mathbf{r}) = \rho_N(\mathbf{r}) - \rho_{N-1}(\mathbf{r})$. In Fig. 5.7 we report $\Delta\rho_N(\mathbf{r})$, as calculated for a few selected cluster sizes. As N increases, the He density smoothly piles up in the main well of the PES, with no visible signature of the secondary, *sub-equatorial*, minimum. The incremental density is mainly localized on the H side of the HCN molecule for N up to 6, mainly on the N side for N between 8 and 14, and nearly isotropically thereafter. Starting from $N \approx 16$, the incremental density shifts toward larger distances from the HCN center of mass (see the inner and the outer contour levels in Fig. 5.7). We consider this behavior as an indication that the first solvation shell is completed around $N \approx 15$, although shell effects are by no means sharp in this system

The dependence of the cluster ground-state energy, $E(N)$, on the size of the system reflects the extremely smooth evolution of the He density profile, as shown in Fig. 5.8 which reports the chemical potential, $\mu(N) = E(N) - E(N-1)$. For

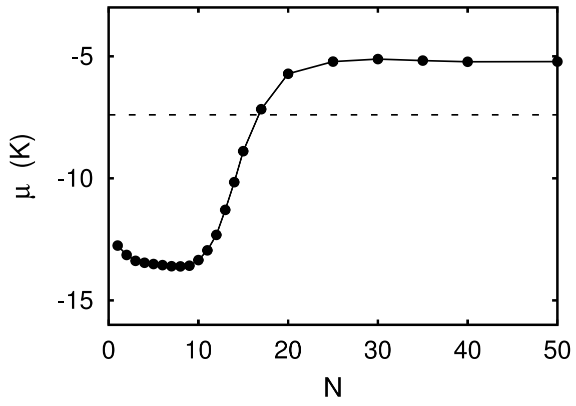

Figure 5.8: Chemical potential, $\mu(N) = E(N) - E(N-1)$, for HCN@He$_N$ clusters. The dashed line is the bulk limit.

N up to a dozen the effect of the He-HCN interaction dominates: the chemical potential stays almost constant, decreasing only very weakly with the cluster size, as a consequence of the He-He interaction. For $12 \lesssim N \lesssim 20$ the first solvation shell is filled and the kinetic energy of He atoms increases due to their closer packing, thus determining a rise of the chemical potential. For $N \gtrsim 20$ $\mu(N)$ is stabilized again at a value which is larger than the bulk limit, due to the smaller effects of the He-He interaction in this size range.

The fact that the first solvation shell is completed in the size range $12 \lesssim N \lesssim 20$ is confirmed by an analysis of the integral M (Eq. 4.3) of the angular correlations of He atom pairs, $C(\phi)$ (Eq. 4.2). M measures the tendency of the He atoms to cluster together on the same side of the molecular axis, due to the He-He attraction (see chapter 4). Fig. 5.9 displays M as a function of N, revealing that this tendency is smallest around $N = 15$, corresponding to completion of the first solvation shell where, for steric reasons, the angular distribution of He atoms around the molecule is most uniform.

5.3.2 Rotational excitations

All the above features of He-solvated HCN molecules are similar to the CO case, already studied in the previous chapter. In Fig. 5.10 we report the energies of the two lowest rotational excitations with angular momentum $J = 1$, along with

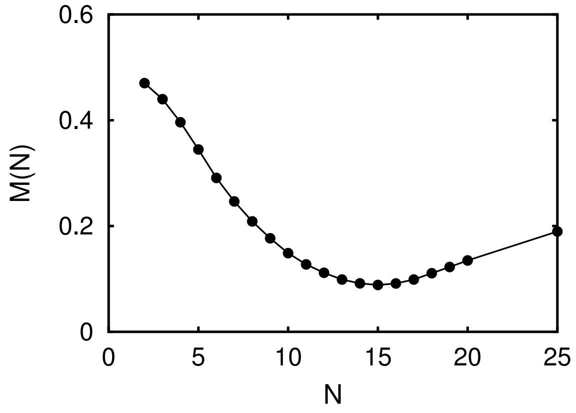

Figure 5.9: Integrated pair distribution of the dihedral angle, defined in Eq. 4.3, as a function of the cluster size, for HCN@He$_N$.

the corresponding spectral weights (Eq.3.17). We note that our predictions for $N > 10$ considerably differ from those of Ref. [14] which were obtained with the POITSE method. This disagreement does not seem to be due to the quality of the potential. The He-HCN interaction used in Ref. [14] is given by the 2E8 PES of Ref. [75]. The latter is an empirical potential, derived from a least-square fitting of a functional form to computational and spectroscopic data relative to HCN@He$_1$ [56]. In order to check if the fitting procedure can make the PES less accurate for larger clusters, we repeated our calculations for few selected sizes, employing the potential of Ref. [75]. In Fig. 5.11 we compare the RQMC results obtained in both cases. Even if, for $N = 14 - 15$, the use of the 2E8 PES shifts the rotational transitions to lower frequencies, the difference with the POITSE result at $N = 25$ persists.

We cannot offer any explanation for this discrepancy. We can only observe that the value of B calculated in Ref. [14] for $N = 25$ is even larger than in the gas phase, a fact that can hardly be explained on physical grounds. In fact, while the reduction of one of the moments of inertia below its value in gas phase—experimentally observed in the binary complex—can be explained by the considerable relative mass redistribution occurring upon formation of the binary complex, similar effects are hard to justify at cluster sizes where the density profile evolves with N in a smooth and almost isotropic way. This seems to suggest that

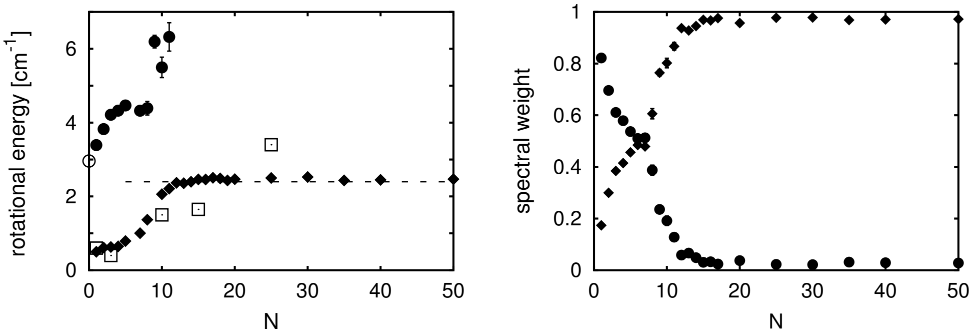

Figure 5.10: Left panel: Rotational energies of HCN@He$_N$ as functions of the cluster size, computed by RQMC (a-type, diamonds and b-type, filled circles); results from the POITSE calculations of Ref. [14] are indicated by squares. The dashed line is twice the effective rotational constant of HCN in the nanodroplet limit [50], while the empty circle at $N = 0$ is twice the gas-phase value. Energy units are cm^{-1}. Right panel: Spectral weight of the a-type line (diamonds) and the b-type line (filled circles).

the results of Ref. [14] may be affected by some inaccuracies for the largest sizes considered in that work. On the other hand, while it is difficult, for large cluster sizes, to ensure full convergence with respect to projection time, as well as full ergodicity in path sampling, we note that the present calculations for HCN are indirectly supported by the agreement between the experiment [5] and similar calculations for the closely related CO-He clusters (see chapter 4).

Two series of excitations, called a-type and b-type lines, evolve smoothly from the known *end-over-end* and the *free molecule* rotational modes of the binary complex, respectively. The b-type line starts off with a stronger spectral weight, then it quickly weakens and eventually disappears. Note how the intensity of the b-type line follows the decline of the He-density angular correlation anisotropy displayed in Fig. 5.9. The existence of two relevant spectral lines (instead of a single line appropriate to the spectrum of an isolated linear rotor) is in fact a manifestation of the dynamical anisotropy of the atomic-density distribution around the molecular axis, which lowers the cylindrical symmetry of the molecular rotor. For $N > 15$ the rise of the He-density angular correlation anisotropy does not give rise to any significant line splitting because it is due to atoms in the second solvation shell, which are only very weakly coupled to the molecular rotation.

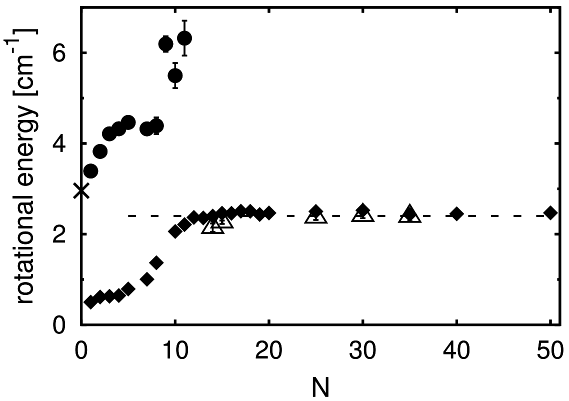

Figure 5.11: Spectral lines, obtained by using the He-HCN potentials of Ref. [65] (diamonds and filled circles correspond to a- and b-type lines, respectively) and of Ref. [75] (triangles).

The coupling between the molecular rotation and He-density fluctuations is better understood using the (imaginary) time correlations $\mathcal{C}_{\mathbf{u}}(\tau)$ of the versor, $\mathbf{u}$, pointing from the molecular center of mass toward the center of mass of the complex of He atoms (Eq. 4.4). Such a time correlation function contains information on the energies and spectral weights of the $J = 1$ cluster excitations whose character is predominantly that of a He-density fluctuation. In Fig. 5.12 we display the lowest-lying excitation energy extracted from the spectral resolution of $\mathcal{C}_{\mathbf{u}}(\tau)$ as a function of the cluster size, and we compare it with the positions of the a-type and b-type lines already reported in Fig. 5.10. We see that this density-fluctuation excitation—which has a relatively strong spectral weight—is degenerate with the a-type line for $N \leq 10$. As in the previous chapter, this mode is interpreted as a cluster excitation in which part of the He density is dragged along by the molecular rotation. For $N > 10$, the energy of this mode departs from the a-type line, and the b-type line correspondingly disappears. This relates to the onset of a situation where the He density is decoupled from the molecular rotation.

We come now to the main concern of this chapter, *i.e.* the convergence of the effective rotational constant to its asymptotic, large-size, value. Our results indicate that the residual renormalization of the effective inertia does not change significantly upon further growth of the cluster beyond, say, $N = 15$. This fact is

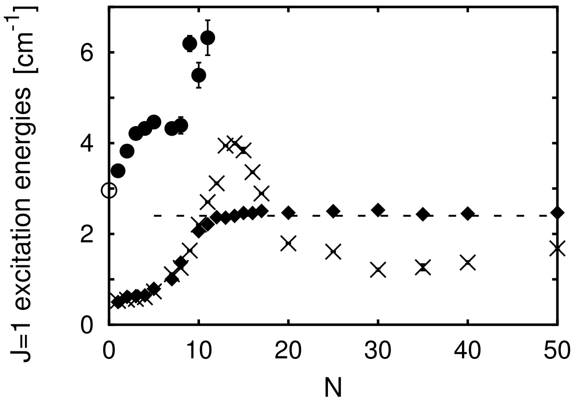

Figure 5.12: Comparison between the positions of the spectral lines reported in Fig. 5.10 (diamonds and filled circles correspond to a- and b-type lines, respectively) with the lowest mode in the spectral resolution of the correlation $\mathcal{C}_{\mathbf{u}}(\tau)$ (crosses, see text).

in complete analogy with the findings reported in chapter 4 for clusters doped with CO (and in agreement high resolution IR spectra recently obtained for He clusters seeded with CO up to $N = 20$ [5]), but at variance with the results reported for HCN in Ref. [14] and with the commonly accepted view. With a similar rotational constant and a similar interaction with He, CO and HCN are not expected to behave very differently upon solvation in He clusters. The experimental results for CO do not seem compatible with a large variation of B between, say, $N = 15$ and 25, thus challenging the idea of slow convergence to the nanodroplet limit as a general feature of the effective inertia of quantum solvated light rotors. Although a conclusive answer will require the measurement and assignment of spectral lines for even larger clusters, we believe that the agreement between our previous calculations and high-resolution IR measurements for the closely related CO@He$_N$ system warrants a considerable trust in the present results and in the conclusions on the approach to the nanodroplet regime based on them.

In conclusion, the results reported here for HCN and in the previous chapter for CO (the latter being supported by the experimental study of Ref. [5]) suggest that for these *light rotors* the asymptotic value of the effective rotational constant is reached well before completion of the first solvation shell. We will see in the next section that this behavior is better attributed to the weak anisotropy of the

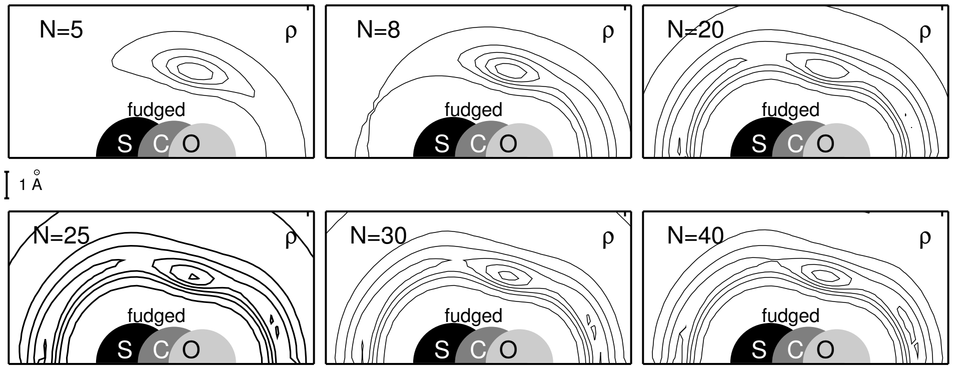

Figure 5.13: He density profiles, ρ_N for various sizes of the f-OCS@He$_N$ cluster. Contour levels start from 0.001 with increments of 0.005, in unit of Å^{-3}. The length scale is indicated by the vertical segment corresponding to 1 Å.

potential, rather than to the small value of B in gas phase.

5.4 Fudged molecules

In this section we consider the fractional reduction of the gas-phase rotational constant B_0 upon solvation in He nanodroplets, $\Delta = B/B_0$. The observed general trend (see e.g. Fig. 13 in Ref. [2]) is that lighter rotors tend to have larger values of Δ. A suitably defined *amount of adiabatic following* [49] has been proposed as the key physical property responsible for the value of Δ (see Sec. 1.3.2). Qualitatively, the analysis of Ref. [49] supports the simple picture that both a small molecular inertia and a weakly anisotropic interaction lead to a large value for Δ. However, there are several exceptions: for instance, N_2O, as shown in Sec. 1.3.2. Therefore, it seems useful to gain further insight by disentangling the role of the PES anisotropy from that of the gas–phase inertia. To this purpose, we have performed simulations with two fictitious molecules: f-OCS (*fudged* OCS), with the PES as OCS and the same B_0 value as HCN, and f-HCN (*fudged* HCN), featuring the HCN–He interaction and the B_0 value of OCS. Note that the gas-phase rotational constants of OCS and HCN are in a ratio of about 1:7.

Fig. 5.13 depicts the He density in f-OCS@He$_N$ clusters. As f-OCS has a larger zero-point energy than the real molecule, the solvent distribution is con-

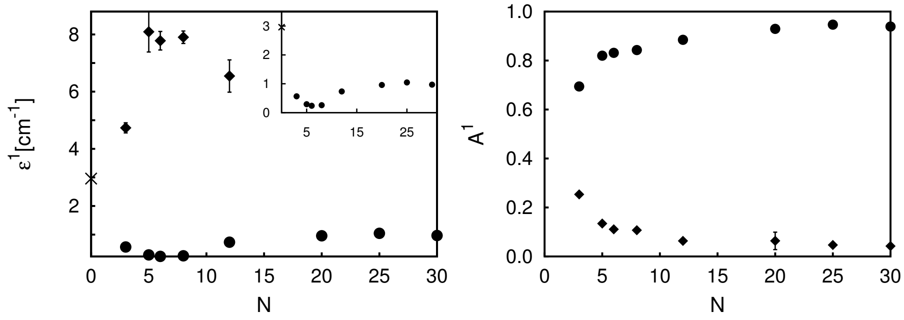

Figure 5.14: Left panel: rotational energies of f-OCS@He$_N$ as a function of the cluster size (a-type, filled circles, and b-type, diamonds). The cross at $N = 0$ shows the fictitious value of $2B_0$. Inset: the detail of the a-type line. Right panel: spectral weights of the a-type line (filled circles) and the b-type line (diamonds) for f-OCS@He$_N$.

siderably more diffuse than in OCS@He$_N$. It can be noted, first, that the full solvation of the impurity occurs at a smaller size, with respect to the real case (see below). Second, the fudged clusters maintain the anisotropic structure of the OCS@He$_N$, even if the density accumulations are less prominent.

Fig. 5.14 shows the rotational energies of f-OCS@He$_N$ (left) and the corresponding spectral weights (right). The general appearance of both quantities for f-OCS is closer to HCN than to OCS, due to the presence of an a-type and a b-type line, with the spectral weight of the latter decaying with increasing N. However, at variance with HCN, the a-type line for large N approaches an energy significantly smaller than the gas-phase value, $2B_0$. Taking the value at $N = 30$ as an estimate (very likely an overestimate, see Section 5.2) of the asymptotic value, we obtain $\Delta \simeq 0.33$, which is close to—and somewhat smaller than—the value of OCS.

The a-type line of f-OCS shows a minimum at $N = 6$ or 7, i.e. at a smaller size than OCS. As shown in Fig. 5.13, already for $N = 8$ there is a significant He density all around the molecule, which is presumably responsible for the turnaround of the B value (although the relation between density profiles and turnaround of the B value could be not so straightforward for f-OCS, due to the residual spectral weight in the b-type line). Regardless of the implications for the turnaround, we stress that the significant difference between the density profiles between f-OCS

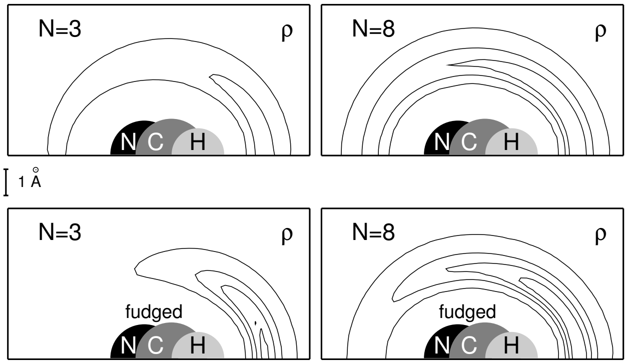

Figure 5.15: He density profiles, ρ_N, for various sizes of the HCN@He$_N$ (up) and f-HCN@He$_2$ (down) clusters. Contour levels start from 0.001 with increments of 0.005, in unit of Å^{-3}. The length scale is indicated by the vertical segment corresponding to 1 Å.

and OCS (see Fig. 5.13) implies a significantly different *amount of adiabatic following*. The fact that the Δ values of f-OCS and OCS are nevertheless very similar, indicates that the anisotropy of the potential, rather than the dynamical regime implied by the gas-phase inertia, is mainly responsible for the renormalization of the rotational constant upon solvation.

Similar conclusions hold for f-HCN as well. A rapid glance at the structure of the fudged f-HCN@He$_N$ clusters evidences that, making the rotor heavier, the solvent can arrange itself in the potential well more easily. In Fig. 5.15 we compare the He density distributions of the fudged clusters with those containing the real HCN molecule. The lower mobility of the heavy f-HCN produces more concentrated density profiles.

The energy of the lowest rotational excitation with $J = 1$, and the corresponding spectral weight, is shown in Fig. 5.16 as a function of N. Already for $N = 3$ the spectral weight of this excitation exceeds 90 percent, and in this respect f-HCN is closer to OCS than to HCN (i.e. the spectrum looks that of a linear rotor for $N \geq 3$).

The different dynamical behavior of f-HCN@He$_N$ with respect to HCN@He$_N$ can be understood by comparing the asymmetry estimator, M, and the rotational energies in the real and in the fictitious cases. In the left panel of Fig. 5.17, we report the M values for the two systems, as a function of the cluster size. It can

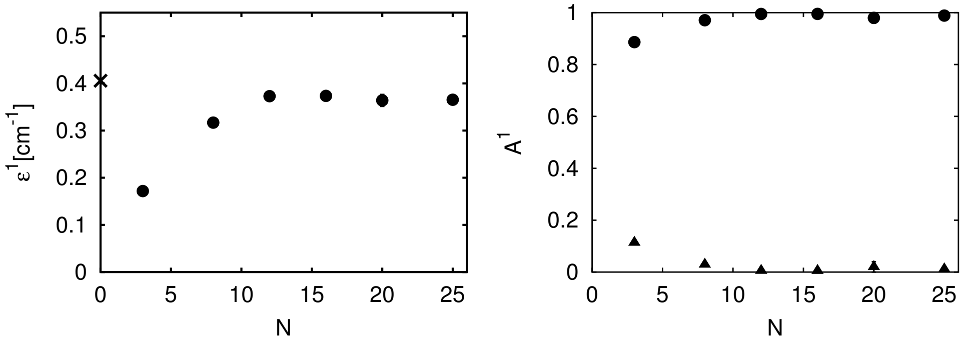

Figure 5.16: Left panel: Rotational energies for f-HCN@He$_N$ (filled circles), as a function of the cluster size. Right panel: Spectral weights of the two lowest rotational energies of f-HCN@He$_N$. Filled circles correspond to the a-type series, triangles to the b-type one(not reported in the left panel).

be noted that the deviation from the cylindrical distribution is quite similar in the two systems. The figure displays also the lowest cluster excitations with $J = 1$ (right). The $\epsilon_{\mathbf{u}}$ series, extracted from the spectral resolution of $\mathcal{C}_{\mathbf{u}}(\tau)$, departs from ϵ_a series as the cluster size increases. The separation between these two modes is significant even at $N = 8$, thus explaining the absence of a second line in the fudged clusters. The values of the $\epsilon_{\mathbf{u}}$ excitations are indeed of the same order of magnitude in f-HCN@He$_N$ and in HCN@He$_N$, while the rotational states of f-HCN lie below those of the real molecule, due to the larger mass of the former.

Thanks to the increased weight, the rotational spectrum of the f-HCN@He$_N$ becomes similar to that of OCS. However, as far as the value of Δ is concerned, the effect of fudging the gas-phase inertia is very small. In order to estimate the asymptotic limit of the rotational constant, we assume that it is given by the value at the largest-size cluster simulated ($N = 25$), noting that the evolution of $B(N)$ in Fig. 5.16 is nearly flat for $N \geq 12$ (for HCN, this assumption would give a very good agreement with the experimental nanodroplet value, see Fig. 5.10). This gives $\Delta = 0.90$ for f-HCN, close to—and somewhat higher than—the value 0.81 measured in HCN [50].

Our findings indicate that the potential alone has a dominant role in establishing the value of Δ, at least in the range of physical parameters appropriate to the linear molecules studied here. Furthermore, the effect of reducing the molecular

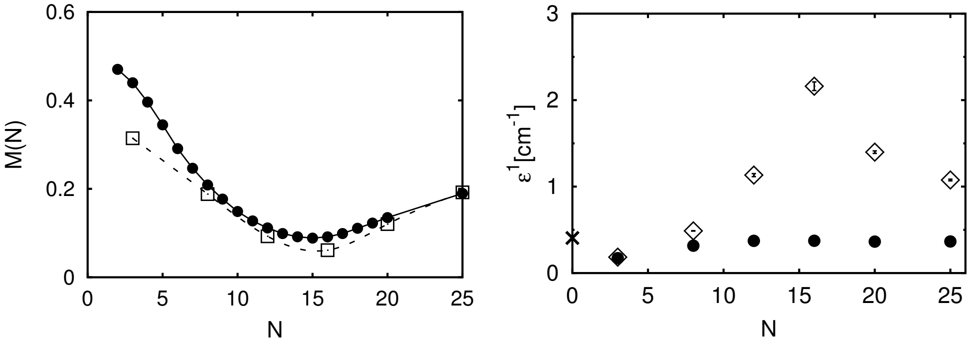

Figure 5.17: Left panel: integrated pair angular distribution, M, as a function of the cluster size, for HCN@He$_N$ and f-HCN@He$_N$ (filled and empty circles respectively). Right panel: Comparison between the positions of the spectral lines reported in Fig. 5.16 (filled circles) with the lowest mode in the spectral resolution of the correlation $\mathcal{C}_{\mathbf{u}}(\tau)$ (diamonds), for f-HCN@He$_N$.

inertia while keeping the PES fixed is to slightly *decrease* the Δ value. This result, in agreement with an experimental study of HCN and DCN [50], contradicts the alleged correspondence between light rotational inertia and large Δ values. We conclude that this correspondence is due, to a large extent, to the generally small anisotropy of the interaction between light rotors and helium—an accidental effect, as far as the rotational dynamics of the solvated molecule is concerned. Within this picture, the behavior of N_2O is *not* an anomalous case, but merely a consequence of the stronger stiffness and anisotropy of the N_2O-He potential with respect to, say, OCS or CO_2.

We finally note that a previous calculation for SF_6 with a fictitiously small gas-phase inertia would support the opposite conclusion that, for given interaction with the solvent, a lighter molecule would have a larger value of Δ [76]. While this result could shed some doubts on the generality of the conclusions drawn from the analysis of a few *linear* molecules, we believe that the calculations of Ref. [76] probably deserve further analysis because they were obtained using a fixed-node approximation, whose accuracy is not warranted, especially for light rotors [14].

5.5 Summary and discussion

Using the RQMC method, we have studied the evolution of the rotational excitations with the number N of solvent He atoms for a prototype heavy rotor, OCS, and a prototype light rotor, HCN. The size range explored, wider than presently attained with number-selective IR and/or MW spectroscopy, allows us to draw a series of conclusions on the approach of the rotational constant to its asymptotic value in the nanodroplet limit. Our results entail a substantial revision, both quantitative and qualitative, of the common view that the asymptotic limit would be essentially determined by the amount of adiabatic following and that—at least for heavy rotors—it would be reached well before completion of the first solvation shell.

The rotational constant of OCS, after the undershoot of the nanodroplet value and the turnaround which signals the onset of superfluidity, crosses again its asymptotic limit at $N = 12$; moreover, starting with the beginning of the second solvation shell around $N \approx 20$, it develops a further structure with an extremely broad maximum, and a faint hint of a (final?) decrease only seen at the largest size we studied, $N = 50$. This feature, which parallels similar findings for CO_2 and N_2O, definitely supports *slow* convergence to the nanodroplet value. A strikingly different behavior is found for HCN. In this case, a linear-rotor-like spectrum is found for N larger than 10, and the resulting rotational constant stays constant in a wide range (say 15 to 50), with a value close to the measured value in the nanodroplet limit. This result contradicts the expectation of a slow convergence to the asymptotic limit (determined by coupling of molecular rotation with well-developed bulk-like excitations of the solvent) as a general property of light rotors. Indeed, a behavior very similar to that illustrated here for HCN was found for another light rotor, namely CO. It would be tempting to propose that *fast* convergence to the nanodroplet limit is a general rule for light rotors. However, recent experimental results [57] indicate that, for CO, the asymptotic limit is significantly lower than inferred from the nearly constant value of the rotational constant in the size range from a dozen to a few tens He atoms. These findings rule out the possibility of defining a general trend for light rotors. In Ref. [57] the different dynamics of CO and HCN in large droplet is related to the different extent of the coupling between the molecule rotation and (discrete) phonon modes.

As already mentioned in the previous chapter, this issue can be seen as a natural prosecution of our work.

In order to establish the relative importance of the bare molecular inertia and of the strength and anisotropy of the He-molecule interaction in determining the approach of the rotational dynamics to the nanodroplet regime, we have also performed computer experiments in which the molecular inertia was intentionally modified. To this end, we have considered two *fudged* molecular species, f-OCS and f-HCN, *i.e.* OCS and HCN with fictitiously small and fictitiously large values of the gas-phase rotational constant, respectively (appropriate in fact to the *other* molecule). Perhaps the most important feature which was attributed to the predominant role of the bare molecular inertia is the amount of renormalization of the gas-phase rotational constant, B, upon solvation: the strong (weak) reduction of B observed for heavy (light) rotors was attributed to the large (small) amount of adiabatic following. Our results indicate that the fractional reduction of the gas-phase rotational constant upon solvation is slightly *stronger* for f-OCS than for real OCS, despite the obvious fact that adiabatic following is much larger for the latter. Likewise, the reduction calculated for f-HCN is somewhat *weaker* for f-HCN than for real HCN. The same trend was experimentally observed, with a smaller variation of B_0, in a comparative study of HCN and DCN [50]. This clearly shows that it is the strength and the anisotropy of the He-molecule interaction, rather than the bare molecular inertia, which is mainly responsible for the renormalization of the rotational constant in the nanodroplet regime. In this perspective, the classification into heavy and light rotors thus retains its validity only to the extent that heavier molecules tend to have stronger and more anisotropic interactions with He.

Conclusions and perspectives

Stimulated by an increasing experimental interest and by some theoretical controversies, we have studied several molecules solvated in He clusters, using the reptation quantum Monte Carlo method. Our work sets up a computational strategy to investigate the dynamics of these systems *(i)* in a wide size and mass range; *(ii)* without any assumption on the relation between structure and dynamics; *(iii)* when the spectra exhibit either a single or a double line.

Rotational energies can be obtained with high accuracy. The agreement with the available experimental data is always remarkable, demonstrating the predictive power of our technique. The effectiveness of the latter is also shown in the calculations of static properties (such as binding energy and density profiles) which cannot be measured experimentally. In particular appropriate estimators have been developed to probe structural asymmetries. Important information on the dynamics of the He matrix have also been derived from unconventional correlation functions, an approach which looks worthy of further attention.

These instruments have been first used to reproduce and interpret the evolution of the rotational spectrum of CO in He clusters, from small to intermediate sizes. Here, a significant insight in the relation between structure and dynamics has been provided. Subsequently we have studied the rotational dynamics of He solvated molecules toward the nanodroplet regime. Here we found unexpected results, mainly the slow approach to the asymptotic limit by heavy molecules, somehow reopening an issue which seemed fully clarified.

Definitely bridging the gap between intermediate size and the nanodroplet regime is a challenging task. This of course requires to access the spectrum of low-lying excitations for larger systems than those studied to date. To this aim the implementation of a ground-state path integral technique, based on the use of the pair approximation to the propagator, has been carried out. The most immediate application would be the study of the rotational spectrum of CO in large droplets, which has indicated a reduction of the rotational constant much larger than inferred from the intermediate size dynamics. These findings, as well as our calculations, demonstrate a non trivial contribution of the outer shells in bringing the rotational constant to the nanodroplet limit. Understanding the nature, the extent of this contribution and its relation with the features of the impurities would be an interesting development of our work.

Appendix A

Pair density matrix approximation

The *action* of a link between two time slices is defined as minus the logarithm of the *exact* quantum propagator:

$$\begin{aligned} S(\mathbf{R}_j, \mathbf{R}_{j-1}; \epsilon) &\equiv -\log\left[G(\mathbf{R}_j, \mathbf{R}_{j-1}; \epsilon)\right] \\ &\equiv K(\mathbf{R}_j, \mathbf{R}_{j-1}; \epsilon) + U(\mathbf{R}_j, \mathbf{R}_{j-1}; \epsilon) \end{aligned} \tag{A.1}$$

wher K is the *exact kinetic action*, as appearing in Eq. 2.7, and U is the interaction term (which is simply $\frac{\epsilon}{2}\left[V(\mathbf{R}_{j-1}) + V(\mathbf{R}_j)\right]$ in the primitive approximation).

Given a system of N particles, interacting via a two-body potential, and with positions $\mathbf{r}_i$ in the time slice $\mathbf{R}$, the pair action approximation is based on the assumption that correlations involving more than two particles can be neglected in the interaction term of the action, U [21]. The latter can thus be written as

$$U(\mathbf{R}, \mathbf{R}'; \epsilon) \simeq U_2(\mathbf{R}, \mathbf{R}'; \epsilon) = \sum_{i<j} u_2(\mathbf{r}_{ij}, \mathbf{r}'_{ij}; \epsilon). \tag{A.2}$$

where $\mathbf{r}_{ij} = (\mathbf{r}_i - \mathbf{r}_j)$ and $u_2(\mathbf{r}_{ij}, \mathbf{r}'_{ij}; \epsilon)$ is the *exact* inter-action for two particles [21], or pair density matrix (PDM).

A.1 Calculating the pair action for spherical potentials

From the computational point of view, it is convenient to evaluate numerically the exact two-body action on a suitable mesh and then interpolate it by a polynomial expression [21]. For *spherical potentials* the procedure is feasible and is implemented in the SQUARER code [77]. The exact two-body action is written through a partial waves expansion [21]:

$$u_2(\mathbf{r},\mathbf{r}';\epsilon) = \frac{1}{4\pi r r'}\sum_{l=0}^{\infty}(2l+1)u_l(r,r';\epsilon)P_l(cos\theta). \tag{A.3}$$

Here θ is the angle between $\mathbf{r}$ and $\mathbf{r}'$. It can be shown that each partial wave verifies the following convolution equation [21]

$$u_l(r,r';\epsilon) = \int_0^{\infty} dr'' u_l(r,r'';\epsilon/2)u_l(r'',r';\epsilon/2), \tag{A.4}$$

which provides the foundations for the *matrix squaring method* [21]. Analytical forms, such as the semiclassical action [21], are accurate in the small time step limit, and they can be used for the partial waves [21]. Therefore, starting from a small time step expression $u_l(r,r';\epsilon/k)$, partial waves $u_l(r,r';\epsilon)$ for any desired time step ϵ, are obtained by squaring $u_l(r,r';\epsilon_k)$ k times, throughout Eq. A.4. Finally the pair action is rewritten in a form which is cheap to evaluate in a Monte Carlo simulation [21]. In particular, three distances are defined [21]:

$$q = (|\mathbf{r}+\mathbf{r}'|)/2, \qquad s = |\mathbf{r}-\mathbf{r}'| \qquad z = |\mathbf{r}| - |\mathbf{r}'|. \tag{A.5}$$

Since they are small (of the order of the thermal de Broglie wavelength, $\sqrt{4\pi\lambda\epsilon}$), the pair action is expanded in a power series of the variables s and z [21]:

$$\begin{aligned} u_2(\mathbf{r},\mathbf{r}';\epsilon) &= \frac{u_{00}(r;\epsilon)+u_{00}(r';\epsilon)}{2} \\ &+ \sum_{k=1}^{n}\sum_{j=0}^{k} u_{kj}(q;\epsilon)z^{2j}s^{2(k-j)}, \end{aligned} \tag{A.6}$$

where the integer n is the *order* of the expansion. The first term on the right hand side is defined *end point action* and corresponds to $n = 0$. The remaining sum

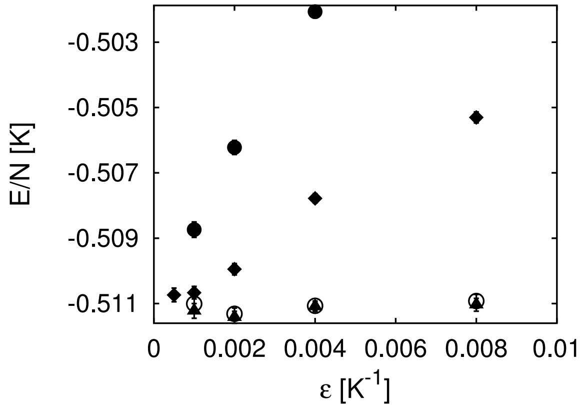

Figure A.1: Convergence of the energy per particle of He$_7$ as a function of the time step ϵ. We report the results of RQMC simulation using the primitive approximation (diamonds), pair action for $n = 0$ (filled circles), $n = 2$ (empty circles) and $n = 3$ (triangles).

contains the *off-diagonal* contributionsi [21]. The code SQUARER [77] provides the tables for the function $u_{ij}(q)$ throughout a least-squares fit to the partial wave expansion. In the study of a given system, the tables are produced once for all before running the QMC simulations. The order in Eq. A.6 has to be chosen by checking the convergence of physical properties for different values of n [21]. Alternatively one can compute the root mean square (rms) error, χ, in converting the exact pair action to the polynomial representation of Eq. A.6. According to Ref. [21], when χ is less than 0.01 most of the measurable quantities are well converged. We have verified that for the He-He interaction of Ref. [78] this condition holds already for $n = 2$. We have tested the correctness of our implementation of the pair action by simulating a cluster of 7 He atoms using RQMC with the PDM approximation. The results are shown in Fig. A.1, where they are compared with those obtained with the primitive approximation. The figure evidences the better quality of the pair action with respect to the primitive one. The off-diagonal terms bring most of the accuracy: the latter is completely lost if the end-point approximation is used, in agreement with previous findings on a two hard spheres system [79]. We also note that when the expansion of Eq. A.6 is taken to order 2 or to order 3 (which requires CPU time 1.6 times longer), no significant difference is observed. The second order is the usual choice for calculations on liquid helium [21]. Since the six terms in the power series share common calculations, the computational demand to evaluate Eq. A.6 for $n = 2$ is only twice larger than for the primitive approximation.

A.2 Pair action approximation for anisotropic potentials

In the case of anisotropic interactions of a linear rotor with helium, a straightforward tabulation of the pair density matrix is not feasible [47, 66]. Because of this, it is convenient to expand the anisotropic potential in a sum of spherical interactions plus a correction term [47, 52, 66]:

$$V(r,\theta) = \sum_{k=1}^{K} V_k(|\mathbf{r} - \mathbf{z}_k|) + \Delta V(r,\theta) \tag{A.7}$$

where $V(r,\theta)$ is the He-molecule potential, $V_k(r)$ is a radial function which describes the interaction of the He atom with a fictitious interaction site $\mathbf{z}_k$, and $\Delta V(r,\theta)$ is the residual term. The functions V_k depend on a set of parameters $\{p_i^k\}$. The values of the $\{p_i^k\}$ and the interaction sites positions $\mathbf{z}_k$ have to be chosen in order to minimize $|\Delta V(r,\theta)|$.

The spherical interactions V_k's can be treated with the pair action, while for the small residual term, ΔV, the primitive approximation is used. Hence, for a doped He cluster of size N, the interaction part of the total action can be written as:

$$\begin{aligned} U(\mathbf{R},\mathbf{R}';\epsilon) &= \sum_{i<j}^{N} u_2^{He-He}(\mathbf{r}_{ij},\mathbf{r}'_{ij};\epsilon) \\ &+ \sum_{k=1}^{K}\sum_{i=1}^{N} u_2^k[(\mathbf{r}_i - \mathbf{z}_k),(\mathbf{r}'_i - \mathbf{z}'_k);\epsilon] \\ &+ \frac{\epsilon}{2}\sum_{i=1}^{N}[\Delta V(r_i,\theta_i) + \Delta V(r'_i,\theta'_i)]. \end{aligned} \tag{A.8}$$

Let us now show the details of this procedure for the He-CO case. For symmetry reasons, the interaction sites $\mathbf{z}_k$ have to be located along the CO molecular

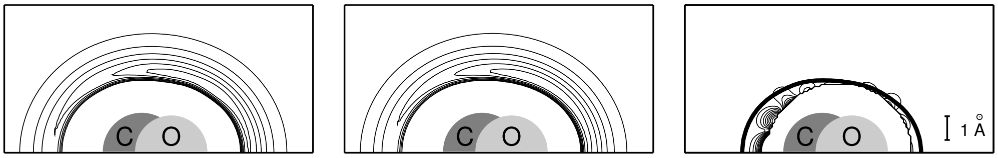

Figure A.2: Left panel: He-CO potential energy surface of Ref. [20]. Central panel: PES resulting from the sum of four spherical potentials of the form described in Eq. A.9 and centered respectively in $\mathbf{z}_1 = (0, 0, 0.05923)$Å, $\mathbf{z}_2 = (0, 0, -0.87619)$Å, $\mathbf{z}_3 = (0, 0, 0.682185)$Å, $\mathbf{z}_4 = (0, 0, -0.0.003240)$Å. The coordinates are in the molecule fixed frame. In the left panel and in the central one, contour levels start from $V = 0$ to negative values and are spaced of 5 K. Right panel: $|\Delta V(r, \theta)|$; contour levels start from $V = 0$ to positive values and are spaced of 2 K. The thick black line indicates the $V = 0$ isopotential line of the true He-CO interaction. For all the panels units on the axis are in Å,

axis. In Eq. A.7, we have used four radial potentials $V_k(r)$ depending on seven parameters:

$$V_k(r) = p_1^k e^{-p_2^k r} + \frac{p_3^k}{r^6} + \frac{p_4^k}{r^7} - \sum_{n=6}^{8} D_n(r) \frac{p_{n-1}^k}{r^n}, \tag{A.9}$$

where the $D_n(r)$'s are the Tang-Toennies damping functions [80]:

$$D_n(r) = 1 - e^{-p_2^k r} \sum_{m=0}^{n} \frac{(p_2^k r)^m}{m!}. \tag{A.10}$$

The various terms of Eq A.9 mimic the repulsion, induction and dispersion contributions appearing in the potentials of van der Waals complexes. In fact, in the choice of the functional form for the $V_k(r)$, we have been guided by one of the analytical expression used to describe the He-HCN interaction [75], which is very similar to that of He-CO [20]. In Fig. A.2 we compare the He-CO PES of Ref. [20] (left panel), with its representation in spherical potentials (central panel). The good quality of the expansion of Eq. A.7 is confirmed by the small anisotropic correction, displayed in the right panel of the same figure. It can be noticed that ΔV is small in the regions physically accessible for He.

The two-body action between a He atom and the k-th interaction site is a function of the reduced mass of the He atom and a fictitious particle in $\mathbf{z}_k$. It is not clear which is the criterion to adopt in choosing the mass of the interaction site. In previous calculations, in which time steps in the range $0.0125 - 0.025$ K^{-1} were used, the sites were supposed to have infinite mass [47, 66]. If we want to include the molecular motion (translations and rotations) it seems more appropriate to use a finite value, *e.g.*, the mass of the CO molecule. For a detailed discussion of the interaction sites expansion see Ref. [72]. We note that the choice of the mass may affect the time step error, but not the zero time step limit of the results.

For each radial potential $V_k(r)$, the matrix-squaring procedure has provided the corresponding density matrix, u_2^k. The latter has been re-expressed throughout the polynomial representation of Eq. A.6 up to the second order. The quality of the power expansion can be judged from left panel of Fig. A.3, which compares the rms error χ relative to the u_2^k's with that of the He-He pair action. χ is about an order of magnitude smaller than the confidence threshold of 0.01. In the right panel of Fig. A.3 we show the u_{00} terms of the two-body density matrices for the He-He interaction [78] and the fictitious spherical potentials.

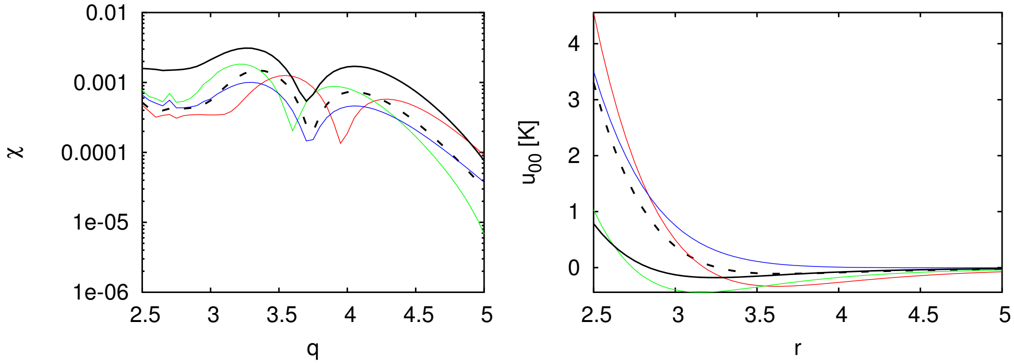

Figure A.3: Left panel: rms error χ in converting the exact two-body density matrices u_2^{He-He} and u_2^k to the second order power series of Eq. A.6. The error is shown as a function of q, after averaging over s and z. Right panel: u_{00} terms of the polynomial expansion of Eq. A.6 for u_2^{He-He} and u_2^k. Distances on the horizontal axis are in Å. The time step is 0.025 K^{-1}. Black solid line: u_2^{He-He}; black dashed line: u_2^1; red line: u_2^2; green line: u_2^3; blue line: u_2^4.

Bibliography

[1] C. Callegari, K. K. Lehmann, R. Schmied, and G. Scoles. *J. Chem. Phys.*, 115:10090, 2001.

[2] J. P. Toennies and A. F. Vilesov. *Angew. Chem. Int. Ed.*, 43:2622, 2004.

[3] S. Grebenev, J.P. Toennies, and A.F. Vilesov. *Science*, 279:2083, 1998.

[4] J. Tang, Y.J. Xu, A.R.W. McKellar, and W. Jäger. *Science*, 297:2002, 2030.

[5] J. Tang and A.R.W. McKellar. *J. Chem. Phys.*, 119:754, 2003.

[6] J. Tang and .R.W. McKellar. *J. Chem. Phys.*, 121:181, 2004.

[7] Y. Xu, W. Jäger, J. Tang, and A. R. W. McKellar. *Phys. Rev. Lett.*, 91:163401, 2003.

[8] S. Grebenev, M. Hartmann, M. Havenith, B. Sartakov, J. P. Toennies, and A. F. Vilesov. *J. Chem. Phys.*, 112:4485, 1999.

[9] C. Callegari, A. Conjusteau, I. Reinhard, K. K. Lehemann, G. Scoles, and F. Dalfovo. *Phys. Rev. Lett.*, 83:5058, 1999.

[10] C. Callegari, A. Conjusteau, I. Reinhard, K. K. Lehemann, G. Scoles, and F. Dalfovo. *Phys. Rev. Lett.*, 84:1848, 2000.

[11] Y. K. Kwon, P. Huang, M. V. Patel, D. Blume, and K. B. Whaley. *J. Chem. Phys.*, 113:6494, 2000.

[12] A. Viel and K. B. Whaley. *Int. J. Mod. Phys.*, 17:5267, 2003.

[13] F. Paesani, A. Viel, F. A. Gianturco, and K. B. Whaley. *Phys. Rev. Lett.*, 90:73401, 2003.

[14] A. Viel and K. B. Whaley. *J. Chem. Phys.*, 115:10186, 2001.

[15] R. Zillich and K. B. Whaley. *Phys. Rev. B*, 69:104517, 2004.

[16] J. Tang, A. R. W. McKellar, F. Mezzacapo, and S. Moroni. *Phys. Rev. Lett.*, 92:145503, 2004.

[17] S. Baroni and S. Moroni. *in Quantum Monte Carlo Methods in Physics and Chemistry*. P. Nightingale and C.J. Umrigar. NATO ASI Series, Series C, Mathematical and Physical Sciences, Vol. 525, (Kluwer Academic Publishers, Boston, 1999), 1999.

[18] S. Baroni and S. Moroni. *Phys. Rev. Lett.*, 82:4745, 1999.

[19] D. Blume, M. Lewerenz, P. Niyaz, and K. B. Whaley. *Phys. Rev. E*, 55:3664, 1999.

[20] T. G. A. Heijmen, R. Moszynski, P. E. S. Wormer, and A. van der Avoird. *J. Chem. Phys.*, 107:9921, 1997.

[21] D. M. Ceperley. Path integrals in the theory of condensed helium. *Rev. Mod. Phys.*, 67:279, 1995.

[22] T. E. Gough, D. G. Knight, and G. Scoles. *Chem. Phys. Lett.*, 97:155, 1983.

[23] D. M. Brink and S. Stringari. *Z. Phys. D.*, 15:257, 1990.

[24] K. Nauta and R. E. Miller. *Science*, 283:1895, 1999.

[25] S. Goyal, D. Schutt, and G. Scoles. *Phys. Rev. Lett.*, 69:933, 1992.

[26] M Hartmann, R.Miller, J. P. Toennies, and A. F. Vilesov. *Phys. Rev. Lett.*, 75:1566, 1995.

[27] J.P. Toennies, A.F. Vilesov, and K. B. Whaley. *Physics Today*, 54:2, 2001.

[28] P. Sindzingre, M. L. Klein, and D. M. Ceperley. *Phys. Rev. Lett.*, 63:1601, 1989.

[29] Y. Kwon, D. M. Ceperley, and K. B. Whaley. *J. Chem. Phys.*, 104:1996, 2341.

[30] Y.J. Xu and W. Jäger. *J. Chem. Phys*, 119:5457, 2003.

[31] S. Moroni, A. Sarsa, S. Fantoni, K.E. Schmidt, and S. Baroni. *Phys. Rev. Lett.*, 90:143401, 2003.

[32] D. Blume, M. lewerenz, F. Huisken, and M. Kaloudis. *J. Chem. Phys.*, 105:8666, 1996.

[33] J.M.M. Howson and J.M. Hutson. *J. Chem. Phys.*, 115:5059, 2001.

[34] S. Moroni, N. Blinov, and P.-N. Roy. *J. Chem. Phys*, 121:3577, 2004.

[35] M. V. Rama Krishna and K. B. Whaley. *Phys. Rev. Lett.*, 64:1126, 1990.

[36] F. Garcias, L. Serra, M. Casas, and M. Barranco. *J. Chem. Phys.*, 108:9102, 1998.

[37] F. Dalfovo. *Z. Phys. D*, 29:61, 1994.

[38] R. N. Barnett and K. B. Whaley. *Phys. Rev. A*, 47:4082, 1993.

[39] F. Dalfovo. *Z. Phys. D*, 14:263, 1989.

[40] F. Ancilotto, E. Cheng, M. F. Cole, and F. Toigo. *Z. Phys. D.*, 98:323, 1995.

[41] F. Stienkmeier, O. Bünermann, R. Mayol, F. Ancilotto, M. Barranco, and M. Pi. *Phys. Rev. B*, 70:214509, 2004.

[42] F. Ancilotto, G. De Toffel, and F. Toigo. *Phys. Rev. B*, 52:16125, 1995.

[43] V. S. Babichenko and Yu. Kagan. *Phys. Rev. Lett.*, 83:3458, 1999.

[44] L. Landau. *J. Phys. USSR*, 5:71, 1941.

[45] L. Landau. *J. Phys. USSR*, 11:91, 1947.

[46] Y. K. Kwon and K. B. Whaley. *Phys. Rev. Lett.*, 83:4108, 1999.

[47] E. W. Draeger and D. M. Ceperley. *Phys. Rev. Lett.*, 90:065301, 2003.

[48] Y. Kwon and K. B. Whaley. *J. Phys and Chem. of Solids*, 66:1516, 2005.

[49] M. V. Patel, A. Viel, F. Paesani, P. Huang, and K. B. Whaley. *J. Chem. Phys.*, 118:5011, 2003.

[50] A. Conjusteau, C. Callegari, I. Reinhard, K. K. Lehmann, and G. Scoles. *J. Chem. Phys.*, 113:4840, 2000.

[51] W. M. C. Foulkes, L. Mitas, R. J. Needs, and G. Rajagopal. *Rev. Mod. Phys.*, 73:33, 2001.

[52] F. Paesani and K. B. Whaley. *J. Chem. Phys.*, 121:5293, 2004.

[53] K. Higgins and W. Klemperer. *J. Chem. Phys.*, 110:1383, 1999.

[54] Y.J. Xu and W. Jäger. *Chem. Phys. Lett.*, 350:417, 2001.

[55] F. Paesani and K. B. Whaley. *J. Chem. Phys.*, 121:10170, 2004.

[56] S. Drucker, F. M. Tao, and W. Kemperer. *J. Phys. Chem.*, 99:2646, 1994.

[57] K. von Haeften, S. Rudolph, I. Simanovsky, M. Havenith, R. E. Zillich, and K. B. Whaley. *Phys. Rev. B*, 73:054502, 2006.

[58] B. L. Hammond, W. A. Lester Jr., and P. J. Reynolds. *Monte Carlo methods in ab initio quantum chemistry*. Singapore World Scientific, 1994.

[59] H. Risken. *The Fokker-Planck equation methods of solution and applications*. Berlin Springer-Verlag, 1989.

[60] H. F. Trotter. *Proc. Am. Math. Soc.*, 10:545, 1959.

[61] A. Sarsa, K. E. Schmidt, and W. R. Magro. *J. Chem. Phys.*, 113:1366, 2000.

[62] C. Pierleoni and D. M. Ceperley. *ChemPhysChem*, 6:1–8, 2005.

[63] P. Nightingale. *in Quantum Monte Carlo Methods in Physics and Chemistry*. P. Nightingale and C.J. Umrigar. NATO ASI Series, Series C, Mathematical and Physical Sciences, Vol. 525, (Kluwer Academic Publishers, Boston, 1999), Sec. III, 1999.

[64] T. Korona, H. L. Williams, R. Bukowski, B. Jeziorski, and K. Szalewicz. *J. Chem. Phys.*, 106:5109, 1997.

[65] R. R. Toczylowskski, F. Doloresco, and S. M. Cybulski. *J. Chem. Phys.*, 114:851, 2000.

[66] R.E. Zillich, F. Paesani, Y. Kwon, and K. B. Whaley. *J. Chem. Phys.*, 123:114301, 2005.

[67] W. L. McMillan. *Phys. Rev.*, 138:A442, 1965.

[68] C. De Michelis and L. Reatto. *Phys. Lett. A*, 50:275, 1974.

[69] C. J. Umrigar, K. G. Wilson, and J. W. Wilkins. *Phys. Rev. Lett.*, 60:1719, 1988.

[70] J. E. Gubernatis and M. Jarrell. *Phys. Rep.*, 269:135, 1996.

[71] W. Janke. Statistical analysis of simulations: Data correlations and error estimation. In Johannes Grotendorst, Dominik Marx, and Alejandro Muramatsu, editors, *Quantum Simulations of Complex Many-Body Systems: From Theory to Algorithms*, volume X, pages 423–445. John von Neumann-Institut für Computing, 548 Seiten, 2002.

[72] See EPAPS Document No. E-JCPSA6-123-043528. This document can be reached from the EPAPS homepage(http://www.aip.org/pubservs/epaps.html) or from J. Chem. Phys. 123, 114301 (2005) via direct link in the online article's HTML reference section.

[73] F. Paesani and F. A. Gianturco. *J. Chem. Phys.*, 116:10170, 2002.

[74] S. Moroni and S. Baroni. *Comp. Phys. Comm*, 169:404, 2005.

[75] K. M. Atkins and J. M. Hutson. *J. Chem. Phys.*, 105:440, 1996.

[76] E. Lee, D. Farrelly, and K. B. Whaley. *Phys. Rev. Lett.*, 83:3812, 1999.

[77] M. Holzmann and C. Pierleoni. *Joint DEMOCRITOS-ICTP School on Continuum Quantum Monte Carlo Methods: Pair density matrix laboratory session. Search in http://cdsagenda5.ictp.trieste.it/*. 2004.

[78] R. A. Aziz and A. R. Janzen. *Phys. Rev. Lett.*, 74:1586, 1995.

[79] G. Jacucci and E. Omerti. *J. Chem. Phys.*, 79:3051, 1983.

[80] K. T. Tang and J. P. Toennies. *J. Chem. Phys.*, 80:3726, 1984.

Acknowledgments

I want to thank Prof. Stefano Baroni, for giving me the opportunity to work here in SISSA on interesting and fascinating subjects, and for showing me that research is a privilege, which deserves passion and devotion. I am deeply grateful to Dr. Saverio Moroni for his precious guide, for the many teachings and fruitful advises. Without him, all this work would have not been possible. I would like to thank Prof. Giacinto Scoles for the useful discussions and for having suggested these studies. I am grateful to Prof. Stefano Fantoni, for his attention in my work and for his encouragement. To my friend Paolo Cazzato I am indebted for the results of some simulations that have been presented in this thesis. I thank Moreno Baricevic and Stefano Cozzini and all the people of the HPC group at SISSA for their technical support in dealing with parallel computing and job running. I am grateful to all the members of SISSA in general, and of the Condensed Matter Sector in particular, for the stimulating environment they create.

I cannot close this section without thanking all the dear friends I have met here, and in particular Alessio, Claudia, Manuela and Osvaldo. Last, but not least, I wish to thank my family for the opportunities they gave me and my fiancée for her lovely support.

Stefano

April 3rd, 2006